High-frequency image analysis of calving activity and styles at Hansbreen, Svalbard

Dhruv MANIKTALA^{1*}, Oskar GLOWACKI¹, Nikola WIERZBICKA-MRÓZ²

¹Institute of Geophysics, Polish Academy of Sciences, Warsaw, Poland

²Faculty of Physics, University of Warsaw, Warsaw, Poland

Correspondence: Dhruv Maniktala <dmaniktala@igf.edu.pl>

ABSTRACT

Sequential photographic records of glacier termini go back to the mid-20th century, revealing climate-driven retreat. More recently, time-lapse imagery has enabled detailed analysis of glacier dynamics, including calving. Here, we use long-term, high-frequency (15 minutes) time-lapse images from May—October 2016 to manually investigate calving activity at Hansbreen, a marine-terminating glacier in Hornsund Fjord, Svalbard. We explore the spatio-temporal variability in calving frequency and styles along the glacier terminus and its relationship to environmental drivers. Average calving frequency was found to be 30 events d⁻¹, and peaking at 60 d⁻¹. The calving activity aligns well with air and ocean temperature at a seasonal scales, while some peaks in calving correspond to increased modelled meltwater runoff and rainfall. These links are inconsistent and reflect high complexity. Calving at Hansbreen varies greatly in time and across five delineated terminus zones. In two of the zones, over 60 % of waterline events occur during ebb tide; these segments also experience regular ice cave formation. However, further efforts are needed to explore the high-frequency evolution of terminus morphology and its link to calving. Our dataset can also be used to train automated algorithms for calving detection from time-lapse imagery.

1. INTRODUCTION

The rapid rise in global temperatures in the early 21st century is largely driven by human activities, with greenhouse gas emissions reaching 59 ± 6.6 Gt CO₂ eq. in 2019, approximately 54 % higher than in 1990 (Mukherji, 2023); this warming extends beyond the atmosphere, as ocean temperatures have risen to record levels since at least the 1950s (Johnson and others, 2021; Cheng and others, 2022). In a much warmer climate, mountain glaciers worldwide are shrinking rapidly, with many projected to vanish by the end of this century (Zemp and others, 2019; Marzeion and others, 2020). The ice loss from the Antarctic Ice Sheet reached ~252 \pm 26 Gt a⁻¹ between 2009-17 (Rignot and others, 2019), while Greenland's ice

This is an Open Access article, distributed under the terms of the Creative Commons Attribution licence (http://creativecommons.org/licenses/by/4.0), which permits unrestricted re-use, distribution and reproduction, provided the original article is properly cited.

loss averaged 286 ± 20 Gt a⁻¹ between 2010-18 (Mouginot and others, 2019); the latter is driven by a nearly balanced contribution from glacier dynamics and surface mass balance (primarily meltwater runoff) (Mouginot and others, 2019; IMBIE Team, 2020). Meltwater runoff is defined as a combination of surface melt and rainfall at the glacier (Van Pelt and others, 2019; Schmidt and others, 2023).

Along with increased surface melting and meltwater runoff, mass loss from ice sheets is also driven by the thinning, acceleration, and retreat of marine-terminating glaciers (King and others, 2020). Marine terminating glaciers are responsible for transporting ice from inner regions of ice sheets or glaciers towards the oceans (Robel and others, 2018). Studies have further shown a positive correlation between rising ocean temperatures and the retreat of glacier termini, emphasizing the role of ocean-driven melting (e.g., Holland and others, 2008; Cowton and others 2018; Wood and others, 2021). Marine-terminating glaciers account for approximately 40 % of the total global glacier area, playing a crucial role in ice mass loss (RGI Consortium, 2017). However, the high complexity of ice/ocean interactions makes it difficult to project ice mass loss at marine margins (Nick and others, 2013; Fürst and others, 2015; Aschwanden and others, 2019). While all glaciers lose mass through surface melting, ice loss from marine-terminating glaciers occurs through frontal ablation, primarily driven by two key processes: submarine melting and glacier calving (Joughin and others, 2004; Nick and others, 2009; Straneo and others, 2013; Luckman and others, 2015).

Calving is defined as the mechanical loss of ice from marine margins of glaciers and ice shelves (Benn and others, 2007). Calving at tidewater glaciers accounts for substantial amount of total ice mass loss; for e.g. in Greenland, calving contributes to nearly 40 % of its annual net mass loss, equivalent to 0.33 mm a⁻¹ of global sea-level rise (Mouginot and others, 2019). In Svalbard, calving accounts for 17–25 % of total mass loss (excluding Kvitøya) (Błaszczyk and others, 2009). In Hornsund fjord, total frontal ablation from marine-terminating glaciers amounts to ~630 Mt a⁻¹, of which Hansbreen contributes ~35 Mt a⁻¹ on average between 2006-19 (Błaszczyk and others, 2019). Mass loss through calving has also been documented in regions such as Patagonia and Alaska (e.g., Venteris, 1999; Motyka and others, 2003; Minowa and others, 2018, 2021). Columbia Glacier has been intensively monitored since its rapid retreat began in 1982, providing valuable insights into calving dynamics and glacier behaviour (e.g., Meier and Post, 1987; Van der Veen, 1996; O'Neel and others, 2005; Walter and others, 2010). In addition to playing a key role in driving ice loss, calving affects the ocean by inducing mixing in the water column (Meredith and others, 2022). However, long-term calving front observations remain scarce (Kochtitzky and others, 2022); this limitation makes it difficult to quantify the relative contributions of calving and submarine melting (Schuler and others, 2020) and fully understand the governing processes (Schuler and others, 2020; Li and others, 2023). Consequently, the spatiotemporal variability of calving and its connections to environmental drivers are not yet fully understood (e.g., How and others, 2019; Kneib-Walter and others, 2021). Despite decades of glacier observations, this knowledge gap persists due to several limitations; the ice/ocean interface is a highly complex environment (see Fig. 6), and the harsh polar conditions make direct observations challenging.

In recent years, numerous studies have focused on quantifying calving. Examples include photogrammetric techniques like time-lapse imagery and terrestrial laser scanning (e.g., Walter and others, 2010; Petlicki and others, 2015; Podgorski and others, 2018; Vallot and others, 2019; Baurley and others, 2022; Ciepły and others, 2023), geophysical approaches such as seismic monitoring, underwater acoustics, and terrestrial radar interferometry (O'Neel and others, 2007; Amundson and others, 2008; Pettit, 2012; Bartholomaus and others, 2015; Podolskiy and Walter, 2016; Glowacki and Deane, 2020; Winberry and others, 2020; Kneib-Walter and others, 2021; Wehrlé and others, 2021), and satellite remote sensing and modeling techniques for large-scale analysis (Greene and others, 2022; Kochtitzky and Copland, 2022; Li and others, 2023). Additionally, tsunami waves generated by calving events were also used to estimate calving fluxes (Minowa and others, 2018, 2019). Of these different observational techniques, the acquisition of time-lapse imagery at calving glacier termini is probably the most widely used.

Time-lapse imagery has been used for decades to monitor glacier dynamics (O'Neel and others, 2003, 2007; Murray and others, 2015), including surface velocity, retreat rates, calving events, and glacier/ocean interactions (Vallot and others, 2019). Its popularity in glaciology stems due to three main advantages: high spatio-temporal resolution, simplicity, and cost effectiveness. Unlike optical satellite imagery, which often suffers from limited temporal resolution and interference from cloud cover, timelapse cameras can be installed close to glacier terminus to capture high resolution images at intervals ranging from seconds to days over extended periods (e.g., Kristensen and Benn, 2012; Petlicki and others, 2015). Camera systems are not only relatively easy to deploy and maintain in the field but also considerably more affordable than many other methods used to collect glaciological data (e.g., Motyka and others, 2003; Ahn and Box, 2010). As a result, some studies from Svalbard have demonstrated the value of time-lapse imagery in monitoring calving. How and others (2019) used high-frequency timelapse photography (one image every three seconds) at Tunabreen, Svalbard, to document calving dynamics over a 28-hour period, identifying individual calving events along with their sizes and styles. Petlicki and others (2015) analyzed time-lapse images at Hansbreen, Svalbard, to show how calving is influenced by local force imbalances at the terminus, caused by the formation of a thermo-erosional notch at the waterline. Despite some important limitations, such as reduced visibility during poor weather and difficulty in detecting submarine calving, methods to automatically identify calving events from timelapse imagery were also developed (e.g., Adinugroho and others, 2015; Vallot and others, 2019).

This study presents a long-term, high-frequency calving dataset for Hansbreen, a tidewater glacier located in the Hornsund fjord of the Svalbard archipelago (see section 'Study Area' for the details of the study site). The primary objectives here were to quantify the variability of calving events in time and along the glacier terminus, and to identify the environmental factors driving this variability. Additionally, one of the goals was to produce a calving dataset that could be used by the community to train automated image processing algorithms. To achieve these goals, we have manually identified and classified calving events using 10,765 time-lapse images of the terminus of Hansbreen, captured at 15-min intervals throughout the 2016 ablation season. Time-lapse images were supplemented by satellite data, along with oceanographic and meteorological observations, to assess the influence of environmental drivers on calving. In the following sections, we first describe the study area, including the glacier and its surroundings, followed by a description of the time-lapse imagery dataset and the methods used to identify calving events and classify their size and style. We then present the spatio-temporal variability of calving frequency along the glacier terminus and explore how this variability relates to environmental drivers acting over short timescales. Finally, we discuss the implications of our findings and evaluate the utility of time-lapse imagery, when combined with observational and modeled environmental data, for studying calving variability.

2. STUDY AREA

2.1 General Setting

Hansbreen is a grounded, tidewater glacier, located in southwest Spitsbergen, Svalbard (see Fig. 1). The glacier is ~14 km in length, and covers an area over 50 km², with the main trunk flowing from North to South (Błaszczyk and others, 2019, 2024; Osika and Jania, 2024). Hansbreen's terminus is 1.5 km wide and has an average height above the waterline of 30 m (Błaszczyk and others, 2009; Glowacki, 2022). In 2015, the average grounding depth along the terminus was approx. 60 m (Błaszczyk and others, 2021), corresponding to a mean ice thickness of ~90 m. The volume and maximum ice thickness (in the upper sections) of the glacier are found to be 9.5 km³ and ~380 m, respectively (Grabiec and others, 2012). Since 1899, the terminus of Hansbreen has been retreating (Błaszczyk and others, 2024). From 1991 to 2015, the glacier's terminus retreated by 900 m (Błaszczyk and others, 2024).

Figure 1 near here

2.2 Climatology and Oceanography

Hornsund is warming rapidly, with an average temperature increase of 1.14°C per decade from 1979 to 2018 with daily mean temperature of -3.7 °C for this period (Wawrzyniak and Osuch, 2020). The precipitation (rainfall) records from the monitoring of the Polish Polar Station Hornsund (PPS, see Fig. 1) for the period 1983-2018 indicate that April and May are relatively dry, while September is wetter, receiving the highest rainfall (Wawrzyniak and Osuch, 2020). The surface meltwater runoff from glaciers, driven by the atmospheric forcing, is responsible for almost 40 % of the freshwater delivery to Hornsund; about 25 % is due to the frontal ablation (Błaszczyk and others, 2019). The frontal ablation of marineterminating glaciers in the fiord is largely controlled by submarine melting (Petlicki and others, 2015; Cieply and others, 2023); this is in line with observations from other regions (e.g. Motyka and others, 2003; How and others, 2019). However, there is no clear trend in the presence of warm Atlantic Water masses in Hornsund despite its southernmost location in Spitsbergen (Jain and others, 2024; Korhonen and other, 2024); this is largely due to the complex interactions between the West Spitsbergen Current and Spitsbergen Polar Current, and the resulting high interannual variability in hydrographic conditions (e.g., Promińska and other, 2017; 2018; Jain and others, 2024). Similarly, there is no clear trend in the sea ice coverage in Hornsund (Swirad and others, 2024). Nevertheless, recent study reported an increased presence of the Atlantic Water close to the fiord's entrance (Strzelewicz and others, 2022); this may suggest that Hornsund can be more sensitive to climate-driven changes in the future.

2.3 Glacier dynamics

Tidewater glaciers, compared to land-based glaciers, generally exhibit high basal velocities year-round (Meier and Post, 1987; Van der Veen, 1996), with increasing velocities near the terminus driven by high water pressure (Kamb and others, 1994; Vieli and others, 2000). A similar increase in velocity near the terminus has also been observed at Hansbreen (Vieli and others, 2000). Hansbreen has been characterized as a slow moving glacier with average annual ice velocities of 100 m a⁻¹ (e.g., Vieli and others, 2002; Błaszczyk and others, 2024). Between 2007-15, average annual velocities 3.5 km upstream from the terminus ranged from 50 to 90 m a⁻¹, whereas near-terminus velocities reached 139 m a⁻¹ in 2013-14 (Blaszczyk and others, 2019; 2021). The ice velocity plays a key role in controlling glacier dynamics; nevertheless, Vieli and others (2002) showed that seasonal changes in the position of the terminus of Hansbreen are driven by calving. Calving activity at Hansbreen has been frequently observed since 1950 (e.g., Jania and Kolondra, 1982; Jania, 1988; Vieli and others, 2002). Over the decades, various tools and methodologies have been used to analyze calving, including terrestrial photogrammetry (e.g., Jania, 1988; Pętlicki and others, 2015; Ciepły and others, 2023), passive underwater acoustics (e.g., Glowacki and Deane, 2020), and satellite remote sensing (e.g., Błaszczyk and others, 2021). Pętlicki and others (2015)

analyzed hourly time-lapse images and found that calving at Hansbreen is largely driven by thermoerosional undercutting at the waterline. Furthermore, the long-term (2011-16) analysis of low-frequency (daily) time-lapse images revealed that different factors can drive seasonal and spatial variability of calving at Hansbreen: sea temperature, activity of subglacial discharges, and the grounding depth (Ciepły and others, 2023). Guided by the results of Pętlicki and others (2015) and Ciepły and others (2023), and the need for better understanding of the event-by-event spatio-temporal variability of calving, we use high-frequency (15-min interval) time lapse images of the terminus of Hansbreen taken in May-October 2016. Details of the image collection and analysis is discussed in the following section.

3. DATA COLLECTION AND ANALYSIS

Figure 2 near here

3.1 Photogrammetry

3.1.1 Time Lapse Imagery

Images of the calving front of Hansbreen were captured at 15-min intervals using a camera positioned on a mountainside approximately 1.4 km southwest of the glacier terminus center (see 'TLC' in Fig. 1). Continuous image acquisition has been ongoing since 2015 as part of a monitoring program conducted by the PPS. For this study, we analyzed images captured between 17 May 2016 and 31 October 2016 using a Canon EOS 1100D camera with a resolution of 4272 × 2848 pixels and an 18 mm focal length. The camera system was equipped with a Harbotronics Digisnap intervalometer and powered by a 12-volt battery in combination with a solar panel. This period was selected because it provided the best data coverage with fewer image gaps from adverse weather or technical issues. In addition, the availability of pressure sensor data for tidal analysis supported the choice of this study period. Each image was timestamped based on the camera's internal clock. However, clock drift occurred over prolonged timelapse photography sessions, a limitation previously documented for consumer-grade cameras in Welty and others (2017). Regular inspections of the camera were conducted by an observer from the PPS to readjust the camera clock and mitigate other technical issues (e.g., power outage, memory card replacement, etc.).

Images with no visibility due to poor weather were removed in pre-processing; this created gaps in data of up to several hours. For each pair of consecutive images, the gap was calculated as a time period exceeding the typical 15-min interval. For example, the interval of 45-min results in a gap of 30-min (45-15). For most of the study period, the camera captured images at the expected 15-min intervals (no gap). Additionally, some data gaps occurred due to unknown technical issues with the camera that

could not be immediately resolved by the observer. Moreover, in the second half of October, image frequency was reduced by 50 % due to the polar night; and during the final six days of October, images were captured at an hourly interval instead of the typical 15-min interval. The mean monthly image gaps for the duration of the study period amounted to approx. 41 %. However, occasional intervalometer malfunctions led to more frequent image captures (e.g., every one or two minutes). These additional images were retained and included in the analysis.

Besides the data gaps, several other issues with time-lapse images were also addressed in post-processing. Factors such as strong winds, precipitation, and occasional human intervention during the memory card replacement caused minor shifts in the camera's position and tilt. These shifts were manually identified using natural control points in the topography, and corrected using IrfanView software to ensure image consistency, an approach also discussed by Harrison and others (2017), for glacier time-lapse monitoring. The images were also cropped to enlarge the view of the glacier terminus, making it clearly visible for identifying and classifying individual calving events. Details of the tilt corrections and cropping parameters are provided in the supplementary material (see Table S1). Furthermore, five equidistant diagonal lines (see Image S1 in supplementary material) aligned with the glacier's flow direction were overlain on all images (see Fig. 2a), dividing the glacier terminus into six zones to assess the spatial variability of calving. However, the easternmost zone six was excluded from further analysis due to the minimal calving activity within its boundaries. Moreover, it is important to note that zone one was only partially visible on camera images.

During manual observation of calving events, several weather-related challenges were encountered. For example, the glacier terminus was often obscured on cloudy and foggy days. Moreover, occurrences of sun glare also posed difficulties by overexposing portions of the images. Despite the reduced visibility, it was usually still possible to detect and document some calving events. To address the visibility-related issues, visual enhancements such as contrast and brightness correction were sometimes necessary to improve the clarity of the glacier terminus (done in IrfanView).

3.1.2 Analysis of Calving – Location, Size, and Style

A total of 10,765 images were manually analyzed for calving events by comparing two consecutive time-lapse images (image pairs) taken 15-min apart. The images were reviewed sequentially in a time-lapse viewer, allowing changes in the terminus to be reliably identified. If the second image showed changes in the features of the terminus (see Fig. 2c-f); such as freshly exposed ice or change in colour/shadow, these changes were recorded as calving events. The presence of glacial ice on the sea surface also served as additional evidence of calving activity. Since the exact moment of each calving event was unknown, the

midpoint between the two consecutive images was used as the event's recorded time. In rare cases, when the intervalometer malfunctioned and images were captured every minute, the event was recorded using the exact timestamp of the image in which it appeared (e.g., for images at 12:01, 12:02, and 12:03, a calving event observed at 12:02 is recorded as 12:02 rather than 12:01:30). This approach maintains consistency across the dataset by reporting all times at the minute level, without including seconds. Each event was then classified based on its location, size, and style. The event location was determined based on manually divided zones (see 'ZI-ZV' in Fig. 2a). If an event occurred at the boundary of two zones, its location is the zone for which the newly exposed area (in pixels) was higher. Calving sizes were categorized into four classes relative to the terminus height above the waterline at the event location: less than 25 % (one), 25 % -50 % (two), 50 % -75 % (three), and greater than 75 % (four) (Fig. 2b). As mentioned earlier, the average terminus height of the glacier is 30 m (Błaszczyk and others, 2009). The heights (H) of newly exposed areas for calving size classes one through four are approximately 7.5 m, 15 m, 22.5 m, and 30 m, respectively (see Table 1). For size classes one, two, and three, we assume an upper bound of H³, allowing these events to be visualized as cubic ice blocks with edge lengths proportional to the fraction of the terminus height. This approach generally overestimates the volume for most events, with exceptions for some very large events. Size class four is not assigned a strict upper bound, as fullthickness or particularly wide events may exceed these estimates. Estimated volume range for each size class is provided in Table 1. Calving events were grouped into four different styles: sheet collapse, submarine, icefall, and waterline (Fig. 2c-f); this is in line with classification applied previously by How and others (2019) and Kneib-Walter and others (2021), with one exception: stack topple events. Due to the 15-min interval between images, it was not possible to differentiate sheet collapses from stack topple events. Consequently, both were classified as sheet collapse in this study. Waterline events involve small ice pieces of sizes one and two breaking off at the waterline. Icefalls occur when blocks of ice, not extending to the waterline, of sizes one, two, and three break off from the subaerial part of the ice front. All events of size four are classified as sheet collapse. Lastly, submarine events were identified when there were no changes in the features of the ice surface above the waterline, but new ice pieces appeared in the water near the terminus. These pieces break off from below the waterline, rising rapidly to the surface and often covered with sediments that give them a darker appearance. An additional fifth category, referred to as the "mixed class", was identified during the classification process. This class represents events where waterline and submarine calving occurred during the 15-min interval between two consecutive images, at the same location. While these mixed events were included in the calculation of total calving frequency, they were excluded from statistical analysis of calving styles due to their very limited occurrence (less than one percent of the total calving events).

Table 1 near here

3.2 Satellite Data

In addition to the time-lapse imagery, satellite data provided complementary information on the spatiotemporal variability of the terminus position. Sentinel-2 images were obtained from the Sentinel Hub web browser, covering the months of May, July, August, and September 2016. True-color images were used, and they were pre-processed in the web browser to enhance brightness, contrast, and sharpness. The spatial resolution of the satellite imagery was 10 m, which allowed for the identification of large-scale changes in the terminus morphology, like the varying width and shape of the terminus. However, this resolution was not sufficient to detect smaller calving events, highlighting the need for time-lapse imagery as the primary tool for monitoring calving events in this study. To ensure the most accurate data, only the satellite images with minimal or no cloud cover were selected for analysis. These images provided clear visibility of the glacier terminus, ensuring that the zone boundaries were delineated as accurately as possible. Further details of the satellite images can be found in the supplementary material (see Table S2). The primary goal of the satellite image analysis was to estimate the width of five zones of the glacier terminus, which were previously applied to time-lapse images (see section 3.1 and Fig. 2a). Identifying the width of the calving terminus in each zone for every month allowed us to normalize the calving frequency estimated from the time-lapse images to the changing width in each zone (bias removal). To accurately delineate the zone boundaries, time-lapse images were used as a reference, with the closest time-lapse image to the satellite acquisition date being selected for comparison. Features on the glacier terminus such as distinct shapes and areas of murky water indicating subglacial discharge, provided key reference points for determining these boundaries. This process was necessary because the shape and location of the calving front changed dynamically during the ablation season, causing the width of the zones to vary over time. As such, the satellite images for each month were analyzed to account for these temporal variations. However, due to the manual nature of the process, an error margin of 100 m is assumed in determining the exact location of the zone boundaries.

3.3 Marine and Meteorological Data

Oceanographic and meteorological data sourced from the PPS database were incorporated into the analysis to explore environmental conditions influencing calving events. To examine temperature and salinity conditions at various depths near the calving terminus of Hansbreen, data from a fixed mooring and CTD casts were utilized ('T' and 'CTD', Fig. 1). The mooring (T) was equipped with RBRsolo-T temperature sensor. It was located approximately 750 m from the calving terminus and deployed at a depth of 40 m, recording ocean temperature every two seconds from 21 July 2016 until the end of the study period.

Salinity and temperature data at multiple depths were obtained from 19 CTD casts conducted at an average distance of 350 m from the calving front. Two different instruments were used: a Valeport miniCTD until 8 June 2016, and a SAIVA/SSTD/CTD-208 thereafter. These casts were performed by an oceanographer from the PPS as part of regular monitoring (see detail in Korhonen and others, 2024). Meteorological data, including daily average air temperature and precipitation, were acquired from a permanent meteorological station at PPS, covering the entire study period. Additionally, modelled meltwater runoff estimates at 250 m resolution were sourced from the outputs of the downscaled model developed by Igneczi and Bamber (2024). The environmental data were processed using Matlab to generate time series, which were then compared to calving frequency on various temporal and spatial scales. For the tidal analysis, the period from 1 July - 30 July, 2016 was selected due to particularly intense calving activity. Sea level data was collected using a water pressure sensor (see 'P', Fig. 1) at onesecond intervals during the first 17-min of each hour (Swirad and others, 2023), and this data was interpolated to provide results at one-minute intervals. The mean sea level was subtracted from the timeseries to obtain tidal amplitude. For each calving event during this time, the tidal amplitude was recorded and categorized into two datasets based on whether the events occurred during ebb or flood tides, excluding those that occurred at the highest or lowest sea level within each tidal cycle. Finally, the bathymetry data for the bay in front of Hansbreen provided information on the variability of water depth along the glacier terminus (see Fig. 1). This dataset was processed using QGIS software and analyzed with Matlab. More details about the CTD cast, pressure data and meteorological measurements are provided in Korhonen and others (2024), Swirad and others (2023) and Wawrzyniak and Osuch (2020), respectively.

4. RESULTS AND DISCUSSION

4.1 Relationship between calving activity and environmental conditions: an overview

Figure 3 near here

Fig. 3 summarizes the calving activity at Hansbreen and the corresponding variability of environmental conditions from May to October 2016. Panel a shows the number of calving events per day (calving frequency), represented by orange dots. On average, the calving frequency during the ablation season of 2016 was 30 d⁻¹, with peak values reaching up to 60 d⁻¹. While data availability is limited in May and June, these months are included to illustrate the increasing calving frequency at the start of the ablation period. Overall, the calving frequency at Hansbreen exhibits substantial variability throughout the ablation season. The blue line in panel a represents the time series of ocean temperature measured at the mooring location (see 'T' in Fig. 1). Although data is only available from mid-July onward, ocean

temperature closely aligns with calving frequency variability. During this period, ocean temperature reaches up to almost 4.5 °C, with a peak around 18 August that coincides with increased calving activity (50-55 d⁻¹). To fill the data gap from May to mid-July, ocean temperature measurements from 19 CTD profiles collected between May and October (approximately 350 m from the terminus; see 'CTD' in Fig. 1) are shown as magenta dots. These profiles reveal a clear warming trend, with median ocean temperatures rising from about –1.8 °C in early May to nearly 4 °C by mid-July. Notably, the CTD-derived temperatures align well with the mooring data from mid-July onward, further supporting the observed relationship between elevated ocean temperatures near the glacier terminus and increased calving activity.

Panel b of Fig. 3 breaks down the total calving frequency into four components, each representing a different event sizes (1 to 4, see also Fig. 2b). In addition, the black line shows the daily cumulative event size, providing a first-order volumetric estimate of calving contributions. Among these, calving events of sizes one and four dominate throughout most of the study period, with typical frequency of around 10 d⁻¹. While a high frequency of smaller calving events is expected, as noted in previous studies (e.g., How and others 2019; Kneib-Walter and others 2021), the substantial contribution from the largest calving events is somewhat unexpected, as fully grounded glaciers like Hansbreen are generally less prone to very large events (Aström and others, 2014). However, given that the time-lapse camera captured images at 15-min intervals, some of these large events may actually represent multiple smaller events that occurred within the time gap but were not individually recorded. This introduces some uncertainty into the results, which unfortunately cannot be fully resolved with the available data. Nevertheless, when considering the cumulative event size, it is clear that the largest events (sizes three and four) contribute the most to total calving volume, even if smaller events are sometimes more frequent or similar in number. Similar patterns, where large events dominate the volumetric flux, have been observed at LeConte and Columbia glaciers, both of which have termini that are floating or close to flotation (Åström and others, 2014; O'Neel and others, 2003). Another interesting observation is the variability in the proportion of different event sizes over time. For instance, between 30 June 2016 and 10 July 2016, calving frequency varies noticeably across all four sizes, whereas from 30 July 2016 to 9 August 2016 and in 18-28 September 2016, calving frequency for all event sizes are much more similar.

Panel c presents the time series of three environmental parameters: precipitation (white bars), air temperature (orange line), and modeled meltwater runoff (blue line). The overall trend of calving frequency appears to roughly correspond with daily average air temperature. At the start of the ablation season, an initial increase in calving frequency coincides with rising air temperatures; this is followed by a relatively stable period around mid-September 2016, then a slight decrease, and finally another peak in

October 2016. However, air temperature alone does not fully account for the high variability observed on shorter timescales, such as daily or weekly fluctuations. Instead, ocean temperature shows a relatively stronger alignment with calving frequency variability (even though not all peaks coincide), suggesting it may be a more important driving factor; this is in line with previous studies conducted at Hansbreen (Pętlicki and others 2015; Ciepły and others 2023). A closer view of the peak alignment is provided in Fig. S1 of the supplementary material. On some instances, the meltwater runoff also correspond with calving frequency; for example, a decline in runoff between 20 July 2016 and 9 August 2016 coincides with a decrease in calving frequency. This aligns with previous studies linking subglacial discharge to variations in calving activity (e.g., Sikonia, 1982; Meier and others, 1985; Meier and Post, 1987; Downs and others, 2023). Howover, while some peaks in precipitation correspond to increased frequency of calving (see, for example, around 19 July 2016 and 17 August 2016), others do not; indicating that short episodes of rainfall, in certain cases, can drive vigorous calving activity at Hansbreen.

4.2 Spatio-temporal variability of calving

4.2.1 Calving Frequency

Building on previous studies that have examined the variability of calving along the glacier terminus (e.g., How and others, 2019; Vallot and others 2019; Wagner and others 2019; Kneib-Walter and others, 2021), here we analyze calving activity at five different zones (see Fig. 2A). Fig. 4 illustrates the spatio-temporal variability of calving frequency at Hansbreen over the study period.

Figure 4 near here

Fig. 4a shows the calving frequency across five zones averaged over five-day periods. Calving frequency in zones I and V usually do not exceed five d⁻¹. Conversely, there are typically at least five events daily at zones II, III, and IV for most of the study period; the maximum calving frequency are observed in zone IV, reaching up to around 23 d⁻¹ in July. Overall, all sections of the terminus experience substantial calving variability over time; this suggests that certain environmental drivers influence calving along the entire terminus, while additional localized factors may regulate calving frequency within specific zones. Examples may include deeper sea beds in zones II, III, and IV (see Fig. 1), potential activity of subglacial discharge plumes at specific locations, spatial variability of ice fragmentation processes, and expected higher velocities in the middle part of the glacier terminus as compared to the edges.

To better characterize the spatial variability of calving activity at Hansbreen, Fig. 4b presents the normalized monthly calving frequency at each zone. The normalization accounts for the zone widths that

are variable over time as the terminus retreats (see section 3.2 for details). Additionally, the black line indicates the duration for which the camera was active in each month (in percentage); this is necessary to account for potential bias associated with the varying number of images used for the analysis. Overall, we observe an increase in calving frequency during the summer months (June-September), which is expected during the ablation season due to higher air and water temperatures (see Fig. 3). In the central zones (II-IV), the typical normalized calving frequency range from 0.02 to 0.03 d⁻¹ m⁻¹. However, there are two exceptions. First, in May the normalized calving frequency does not exceed 0.01 d⁻¹ m⁻¹ in any of the zones; this suggests that the ablation season at Hansbreen started in June this year. Second, a particularly high calving frequency is observed in zone II in October; this could be due to (i) potential high activity of subglacial discharge plume in zone II resulting in terminus undercutting (Motyka and others, 2003; see also elevated rainfall in October in Fig. 3c) and (ii) the bias associated with lower image frequency in second half of October compared to July, August and September (see section 3.1.1 for details). The image coverage is high in July-September (75-95 %), while in May-June and October it drops to 20-40 %; this is largely due to technical issues with the camera (May-June) and previously mentioned lower image frequency in October.

4.2.2 Calving styles

Fig. 5 illustrates the calving frequency across four distinct styles and its variability over time and along the terminus (see Fig. 5a and 5b, respectively). Fig. 5a highlights the evident contrast in calving frequency among the four styles. Sheet collapse and waterline events dominate throughout the study period, averaging 15 d⁻¹. Conversely, icefall and submarine events occur far less frequently, averaging only two—three d⁻¹. Guided by previous studies, the high frequency of waterline events was expected; for example, How and others (2019) reported a dominance of waterline events at Tunabreen captured with time-lapse imagery at three-sec intervals. However, our study shows that at Hansbreen sheet collapses occur just as frequently as waterline events; this is likely due to the lower image frequency compared to the study by How and others (2019). We assume that at least some fraction of events classified as sheet collapses were in fact composed of multiple low-magnitude events not captured at 15-min interval imagery. Unfortunately, this limitation cannot be resolved without a new set of data. The overall high frequency of waterline events is likely associated with high melting at the waterline, as previously observed at Hansbreen by Pętlicki and others (2015) and Ciepły and others (2023). However, when considering the cumulative event size (Fig. 5a, black line), it is evident that sheet collapse events contribute more to the total (estimated) calving volume than waterline events, despite similar or slightly lower frequencies.

Figure 5 near here

Fig. 5b presents the percentage distribution of calving styles across different zones over the entire study duration. Notably, the proportion of dominant waterline events increases from 35 % in zone I to 46 % in zone V. A similar pattern is observed for icefall events. Conversely, the percentage of submarine events decreases from 20 % in zone I to less than 1 % in zone V; this is likely due to increasing distance from the camera and the associated difficulty in recognition of such events (no changes at the visible part of the terminus). As a result, the number of submarine events in zone V is almost certainly underestimated, which may also partially explain a higher proportion of waterline and icefall events in this zone. Recent studies using geophysical techniques such as underwater passive acoustics have improved the detection of submarine events (Glowacki 2022); such methods could work in tandem with time-lapse imagery. Sheet collapse events are more frequent in zone II, III, and IV; this is in line with previous observations by Petlicki and others (2015), which indicate a relationship between sheet collapse and deeper sea beds (see bathymetry in Fig. 1). To complement this percentage-based view, we additionally present a first-order volumetric perspective in the supplementary section (see Fig. S2), showing the cumulative event size distribution across zones. This analysis highlights that, although waterline events dominate numerically in some zones, sheet collapse events (sizes three and four) account for the bulk of calving volume, with Zone IV exhibiting the highest estimated volumetric discharge and Zone I the lowest. Integrating this volume-weighted perspective with the event-count percentages provides a more comprehensive understanding of calving variability along the terminus width.

4.3 Driving factors

As shown in our results, calving frequency at Hansbreen exhibit spatial and temporal variability. A complex relationship between the calving frequency and styles and various environmental parameters indicates that calving is not driven by a single factor (see Fig. 3,4, and 5) (e.g., Venteris and others, 1999; Motyka and others, 2003; O'Neel and others, 2003). Instead, a combination of factors influences calving at different locations along the terminus width over varying time periods; this is not surprising, as previously demonstrated for other tidewater glaciers (How and others, 2019; Kneib-Walter and others, 2021). Several atmospheric and oceanographic processes are illustrated schematically in Fig. 6 to better understand the potential drivers of high spatio-temporal variability of calving at Hansbreen. Fig. 6a shows a front-facing, quasi-three-dimensional view of the glacier bay along with different environmental factors varying along the terminus width: ice velocity (higher in the central region and lower towards the edges), seabed geometry, and localized freshwater discharge plume. It also depicts the division of the glacier terminus into five distinct zones (see section 3.1.2), and average depth of the sea bed in each zone. Fig. 6b focuses more on the processes that can be assumed to evenly influence the entire glacier terminus: weather conditions (air temperature, precipitation, solar radiation), advection of warm water masses at

depth and mixing, periodic changes of the sea surface height (tidal cycle), and wind driven surface waves. It is difficult to accurately quantify the individual impact of each environmental driver on calving due the fact that these drivers themselves are interdependent. However, we will now discuss some important processes (and their interdependencies) that influence calving at the ice/ocean boundary.

4.3.1 Processes and relationships: an overview

Interactions between glaciers and the ocean are strongly influenced by processes occurring at (the surface) and within the glacier. One example is the production and drainage of meltwater. Recent studies have shown an increase in the modelled runoff from glaciated regions in Svalbard in the past few decades, which was found to be primarily driven by the enhanced summer melt (Van Pelt and others, 2019; Schmidt and others, 2023). As explained by Scambos and others (2000), and Hagen and others (2003), surface meltwater drains into the cracks, crevasses, and moulins in the ablation zone of the glacier. The presence of water in the glacier system impacts calving in two different ways.

First, crevasses filled with water can further deepen and reach the sea surface level (Van der Veen, 1998), increasing the calving rate (crevasse-depth calving criterion; Benn and others, 2007). Second, the glacier velocity increases with the increasing amount of surface meltwater reaching the glacier bed (Vieli and others, 2000; O'Neel and others, 2005). Indeed, Vieli and others (2004) revealed persistently high basal sliding rates in the ablation zone of Hansbreen throughout the year, with enhanced velocities near the glacier terminus; similar observations are reported from other regions than Svalbard (e.g., Krabill and others, 1999 for Greenland). Higher flow velocities facilitate crevassing and increase the ice flux towards the terminus, both of which promote calving (e.g., Van der Veen, 1996; Vieli and others, 2000; Schild and others, 2018).

Figure 6 near here

Along with the increase in velocity close to the terminus, studies have also shown increased subglacial discharge following the summer glacier melt (e.g., Joughin and others, 1996; Motyka and others, 2003; Chu and others, 2009) The subglacial discharge can be highly variable in terms of the amount of water transported, location, and timing, depending on the surface melt rate and spatio-temporal evolution of the drainage system (Vallot and others, 2017; Schild and others, 2018). The outflow of subglacial water at depth promotes mixing of the water masses through upwelling and enhances submarine melt at the glacier terminus (Motyka and others, 2003; Cowton and others, 2015). The increased melt at the discharge location undercuts the terminus and thereby drives calving (Vallot and others, 2017; Everett and others, 2021). The undercut depth depends strongly on the properties of the ambient waters; Carroll and others (2015) suggested that the degree of ocean stratification impacts the

neutral buoyancy depth to which the plume rises. Increased calving at locations of active subglacial plumes have been widely reported in different regions; examples include Svalbard (Schild and others, 2018; How and others, 2019) and Greenland (Kneib-Walter and others, 2021).

Another factor impacting the calving rates at marine-terminating glaciers is the variability of the thermohaline structure of the ocean (e.g., Rignot and others, 2010; Luckman and others, 2015; Holmes and others, 2019). Besides the short-term and seasonal changes of the hydrography (driven largely by local environmental conditions), the fjords along the west coast of Spitsbergen can be influenced by the warm Atlantic water masses (e.g., Schauer and others, 2004; Strzelewicz and others, 2022, Jain and other, 2024). The Atlantic waters may interact with the submarine part of the glacier terminus, potentially promoting melting followed by undercutting, and thereby enhancing calving (e.g., How and others. 2019; Truffer and Motyka, 2016; Rignot and others, 2015). However, the presence of the sill may limit or restrict the inflow of warm water masses towards the terminus (e.g., Bao & Moffat, 2024; Carroll and others, 2017).

While the sill depth is one important geometric control on the water intrusion into glacier bays, the water depth at the glacier terminus also influences the calving behavior. For example, Brown and others (1982) and Pelto and Warren (1991) found a linear correlation between the water depth and calving activity (rate/flux); Van der Veen (1996) and Vieli and others (2001) reported that the retreat of marine-terminating glaciers can be largely driven by changes in bed topography. Although our study focuses on calving frequency, we also observe spatial variability that may reflect bathymetric controls; specifically, more calving events in the central portion of the glacier terminus compared to the edges, which may be related to the deeper water in zones two, three and four compared to zones one and five.

In addition to the bathymetry, wind driven surface waves and tides can potentially influence calving by promoting erosion and force imbalance at the terminus. Several authors reported a relationship between tidal phase and variations in calving size and style (e.g., Holmes and others, 2023; How and others, 2019; Bartholomaus and others, 2015). This relationship is discussed in detail in the following section.

4.3.2 The role of tides

To investigate the role of tides in controlling calving frequency at Hansbreen, we related the pressure sensor data with the outputs of the image analysis for the month of July (see section 3.3 for details); Fig. 7 summarizes the results of this exercise. Fig. 7a shows the proportion of calving events of different styles observed during the ebb and flood tides. Waterline events show the strongest asymmetry, with 56 % of events occurring during the ebb tide. In contrast, icefall events exhibit the opposite pattern, with 53 % of

events occurring during the flood tide. There is no tidal dependence on the number of sheet collapse events. Previous studies suggested some preference of calving events to occur during the ebb tide. For example, Bartholomous and others (2015) and Holmes and others (2023) showed that large calving events are occurring more often during the falling tide at Yahtse Glacier (Alaska) and Kronebreen (Svalbard), respectively; similar observation was reported by How and others (2019) for Tunabreen regardless of the calving style. The conclusion from these studies was that deeper water has a stabilizing effect on the glacier terminus. However, it is unlikely that the decrease of the backstress during the ebb tide would solely affect waterline events (as observed in our case). Given the significant tidal influence on waterline events at Hansbreen, further results primarily focus on this calving style (see Fig. S3 in supplementary material for other styles).

Figure 7 near here

The histogram in Fig. 7b relates the number of waterline calving events and the tidal amplitude, irrespective of tidal phase. The lowest number of calving events (less than 10 d⁻¹) are observed close to high and low tides, for which the change in water level is expected to be more gradual. Conversely, it seems that more abrupt changes in the water level result in an increased number of calving events (around 90 d⁻¹ between -0.5 and 0.5 m, see Fig. 7b). We hypothesize that the drop of the sea surface height can potentially destabilize the lowest parts of the glacier terminus by reducing the buoyancy of the fragmented ice pieces.

The proportion of waterline calving events occurring during ebb and flood tides varies along the glacier terminus, as represented by the pie charts in Fig. 7c. In zones II and V, 61 % of waterline events occur during ebb tide, while this number drops to 52-53 % in zones I, II, and IV; this indicates that (i) the dependency of waterline events on the tidal cycle is not homogenous along the glacier terminus, and (ii) there is an apparent localized driver(s) of calving in zones three and five.

We hypothesize that the presence of subglacial discharge plumes might be the reason for increased calving frequency at specific zones; such a relevance has also been suggested in previous studies. Early work in Alaska linked seasonal variations in calving velocity within embayment at glacier termini to subglacial runoff (e.g. Sikonia, 1982; Meier and others, 1985). Furthermore, Motyka and others (2003, 2013) demonstrated that subglacial discharge drives submarine melt at LeConte glacier, thereby promoting calving. Building on this foundation, recent studies have observed similar patterns at other locations. For example, Schild and others (2018) and How and others (2019) showed increased calving activity at the locations of discharge plumes at Kongsbreen and Tunabreen (Svalbard), respectively. Moreover, Cook and others (2021) found a 70 % increase in the number of calving events at

Sermeq Kujalleq (Greenland) at locations of meltwater plumes; however, these were mostly small-size events. Higher calving activity was also observed at the locations of meltwater plumes at Eqip Sermia, Greenland (Wehrlé and others, 2021). We looked again at the time-lapse images from July 2016 to explore the potential relationship between the plume locations and frequency of waterline calving events. The assumption was that the presence of cave-like formations at the waterline (ice cavities) may indicate the activity of discharge plumes. Ice cavities follow a cyclic pattern; they form and expand as small ice fragments detach from the terminus, eventually collapsing and reforming. In July 2016 we observed clear ice cavities in zones III and V (see Fig. 8), which corresponds to the highest occurrence of waterline events (see Fig. 7c). It may suggest the complex relationship between the expansion of ice cavities and the destabilizing effect of the falling tide (discussed previously). Despite limitations due to the low camera angle, ice debris, and variable optical conditions, plume activity was visible in some locations on some days in July. Most consistently, plumes were observed at the border of zones III-IV and in zone V. The plume at the zone III-IV border corresponds with an embayment at the glacier terminus, while the plume in zone V aligns with one of our identified ice cavities. Occasional plume activity was also noted in zone I. These observations indicate that plumes are present at multiple sites, although they may not always appear at the surface, likely because they reach the depth of neutral buoyancy (Carroll and others, 2015). The prominent plume locations identified in July 2016 from both satellite and time-lapse imagery are shown in supplementary material (Fig S4).

Figure 8 near here

The tidal cycle is associated not only with the variability of the water level (vertical movement), but also with tidal currents (horizontal movement); the horizontal water flow definitely impacts the submarine melting and melt undercutting of the glacier terminus due to the water advection and mixing (see, e.g., Holmes and others, 2023). However, we are not in a position to speculate about the influence of the tidal currents on the calving activity due to the lack of dedicated measurements.

4.4 Challenges and future needs

Despite recent advances in using time-lapse imagery to quantify the spatiotemporal variability of calving, some challenges still remain in capturing the fine-scale dynamics at the ice/ocean interface (Kneib-Walter and others, 2021); these difficulties are largely compounded by complicated logistics in harsh Arctic conditions. Time-lapse cameras often suffer battery failures in extreme cold, and image quality is frequently degraded by cloud cover, fog, rain, or wind-driven shifts in camera orientation (How and others, 2019; Vallot and others, 2019). Enhancing time-lapse imagery for calving studies requires improved power systems, more reliable intervalometers, and higher image capture frequency to resolve

individual events more effectively. Moreover, time-lapse images become useless during the polar night, and remote locations of glacierized bays often prevent regular inspections of the camera systems. Importantly, time-lapse observations of calving events should always be supplemented with other measurements to better understand environmental drivers and complex interactions between different processes (interplays between the atmosphere, ocean, and glaciers).

Long-term meteorological data from the PPS reflects general weather patterns in southern Svalbard (Wawrzyniak and Osuch, 2020), but these measurements are likely not representative for local conditions in glacial bays driven by topographic factors (e.g., glacier geometry, shape of the coastline, level of isolation by mountain ridges). Moreover, the three-dimensional structure of the ocean temperature, salinity and currents is often sampled at sparse locations and with low temporal resolution; examples include infrequent CTD casts, point measurements by moored systems, and sporadic active acoustic sensing of ocean mixing and activity of subglacial plumes. In situ oceanographic measurements near glacier termini are further restricted by the dangers of navigating boats among icebergs and the risk of sudden calving events. As a result, our understanding of ice/ocean interactions that drive calving is still limited (e.g., Straneo and Cenedese, 2015; How and others, 2019; Kneib-Walter and others, 2021). Furthermore, some glaciological measurements also remain difficult and constrained. For example, ice velocity is usually measured with stakes mounted far from the glacier terminus at a few specific locations (e.g., Blaszczyk and others, 2024); as a result, detailed observations of velocity variability along the terminus width remain limited. Overall, measurements of atmospheric, oceanic, and glaciological drivers are crucial to better understand the spatio-temporal variability of calving (e.g., heterogeneity along the terminus, seasonal cycles, calving styles).

Integrating time-lapse imagery with simultaneous data from passive underwater acoustics, satellite imagery, and other geophysical tools can significantly improve event detection and interpretation (e.g. Glowacki and others, 2015; Li and others, 2023). For meteorological monitoring, deploying automated weather stations closer to glacier terminus would enable better detection of microclimatic conditions and their influence on calving activity (e.g., Kneib-Walter and others, 2021). In the ocean, it is impossible to perfectly characterize the complex three-dimensional environment. However, including numerical models or conducting more frequent CTD and active acoustic measurements along glacier termini certainly helps to better characterize the mixing of different water masses and identify subglacial discharge locations (e.g., Mankoff and others, 2016; Jackson and others, 2017; Schild and others, 2018), both of which are critical for understanding ice/ocean interactions and their role in calving variability. Moreover, expanding the multi-sensor approach to multiple glacier bays within the same fiord (or system

of fiords) would improve our understanding on the impact of site-specific conditions on calving (e.g., glacial and bay geometry).

Meanwhile, recent technological advancements, including drone-based data collection and active acoustic sensing, have already provided valuable insights into calving dynamics. UAVs and aerial drones, for example, have been successfully used to reconstruct 3D structures of glacier terminus and icebergs through structure-from-motion photogrammetry, providing insights into the ice geometry and calving fluxes (e.g., Westoby and others, 2012; Ryan and others, 2015). Similarly, active acoustic techniques have proven effective in mapping the submerged parts of glacier termini and subglacial discharge plumes (e.g., Weidner and others, 2024; Sutherland and others, 2019), and passive underwater acoustics show promise for remote monitoring of calving fluxes and styles (Glowacki and Deane, 2020; Glowacki, 2000). Furthermore, recent advances in marine robotics have demonstrated their value in collecting data close to the ice/ocean interface, such as near-glacier bathymetry, ocean temperatures, and subglacial meltwater plumes, using tools like Autonomous Underwater Vehicles (AUVs) and Unmanned Semi-Submersible Vehicles (USSVs) (Howe and others, 2019; Bruzzone and others, 2020).

Artificial intelligence and machine learning approaches have shown promise in automated calving detection from time-lapse imagery (Vallot and others, 2019; Adinugroho and others, 2015); however, these techniques face challenges such as false positives, variable lighting conditions, and obstructed glacier views. As a result, manual image analysis still remains more reliable. Moreover, automated techniques require high-frequency, long-term training datasets of manually-identified calving events; such a dataset is provided here. A model trained on these data is expected to be most applicable to glaciers with Hansbreen-like characteristics: relatively small, fully grounded tidewater glaciers with terminus widths under ~3 km, average terminus heights (above the waterline) up to 50 m, frequent small calving events, and rare or absent full-thickness failures, where calving is strongly influenced by waterline melting. We do not anticipate such a model would perform well for ice shelves or for the much larger tidewater glaciers of Greenland or Antarctica, where calving styles are fundamentally different and dominated by large tabular iceberg production. Nevertheless, the dataset presented here could provide a valuable foundation for model adaptation to other glacier settings.

5. CONCLUDING REMARKS

In this study, we analyzed the calving activity at Hansbreen using a dataset of over 10000 high-frequency (15 minutes) time-lapse images captured between May and October 2016. By manually identifying and classifying almost 3300 calving events based on their location, size, and style, we offer new insights into the calving variability at Hansbreen (spatial and along the glacier terminus). The integration of calving

data with environmental observations allowed us to assess the potential drivers influencing calving variability. Our findings reveal that calving frequency at Hansbreen vary both spatially and temporally, with an average frequency of approximately 30 d⁻¹ during the 2016 ablation season and peak frequency reaching 60 d⁻¹. Throughout the study period, calving events of lowest and highest magnitude were most common, occurring at typical frequency of 10-15 events per day. While frequent small calving events are expected (How and others 2019; Kneib-Walter and others 2021), the notable contribution from larger events was more surprising. This may, in part, be due to the 15-min interval between images, which could result in multiple smaller events being grouped into single, larger observations. Among the calving styles, a similar uncertainty applies to the frequent sheet collapse events. Waterline calving events were particularly common and are likely linked to enhanced melting at the waterline, in line with previous observations at Hansbreen (Petlicki and others 2015; Ciepły and others 2023). By considering both the size and style of calving events, a first-order volumetric assessment shows that sheet collapse events, which consist primarily of the largest size classes, dominate the total calving volume, even though smaller waterline events occur at a similar frequency. This highlights spatial variability, with the highest volumetric discharge observed in zone IV along the terminus. In two zones of the glacier terminus, more than 60% of waterline calving events occurred during ebb tide, in areas where ice caves form regularly, suggesting presence of subglacial discharge plumes at these locations. The relationship between calving frequency, calving styles, and environmental drivers appears complex. Overall, the calving frequency correlates with air and ocean temperature on seasonal scale; however, these environmental drivers (either individually or collectively) do not fully explains calving variability, likely due to their interdependence and the influence of additional, unmeasured processes. The high temporal resolution and detailed manual classification of our dataset offer valuable potential for future applications. Specifically, this dataset could serve as training data for the development of automated algorithms aimed at detecting and analyzing calving events from time-lapse imagery.

CONTRIBUTION STATEMENT

DM manually processed the time-lapse images, analyzed most of complementary data, participated in formulating research objectives, and wrote the first draft of the manuscript as part of his PhD study. NWM analyzed the tidal data during her internship. OG conceived the study, obtained funding, supervised DM and NWM, and participated in data collection. All authors contributed to the interpretation of results and writing of this article.

DATA AVAILABILITY STATEMENT

All datasets used in this study are publicly available or included as supplementary material. The timelapse images are available at

https://geodata.igf.edu.pl/Dataset_timelapse_photos/Fugle_107_to_Hansbukta/2016/. Ocean temperature from CTD casts was obtained from station 'HB01' and is accessible via Korhonen and others (2024): https://geodata.igf.edu.pl/Dataset_CTD_raw/2016/. Modelled meltwater runoff data were derived from Igneczi and Bamber (2024) and are available at https://doi.pangaea.de/10.1594/PANGAEA.967544. The bathymetry map was obtained from Błaszczyk and others (2021), available at https://ppdb.us.edu.pl/geonetwork/srv/eng/catalog.search#/home. Sea level data, from which tidal information was derived, were obtained from a pressure sensor at station 'HBK7' and are available in Świrad and others (2023): https://doi.pangaea.de/10.1594/PANGAEA.954201. Satellite imagery used in this study was downloaded from https://apps.sentinel-hub.com/eo-browser/. Additionally, datasets related to calving classification, moored ocean temperature, air temperature, and precipitation are provided as supplementary material.

SUPPLEMENTARY MATERIAL

The supplementary material for this article can be found at [LINK].

ACKNOWLEDGEMENTS

This study has been supported by the National Science Centre, Poland (grant 2021/43/D/ST10/00616) and the Ministry of Science and Higher Education of Poland (subsidy for the Institute of Geophysics, Polish Academy of Sciences). We would like to thank Prof. Mateusz Moskalik for setting up the photographic monitoring of Hansbreen. We are also grateful to the team members of the Polish Polar Station Hornsund for their support during fieldwork. We would also like to thank the handling editor Dr. Shad O'Neel, and the two anonymous reviewers, whose suggestions have greatly improved this manuscript.

REFERENCES

Adinugroho S, Vallot D, Westrin P and Strand R (2015) Calving events detection and quantification from time-lapse images in Tunabreen glacier. *International Conference on Information & Communication Technology and Systems (ICTS)* 61-66 IEEE. doi:10.1109/ICTS.2015.7379872

Ahn Y and Box JE (2010) Glacier velocities from time-lapse photos: technique development and first results from the Extreme Ice Survey (EIS) in Greenland. *Journal of Glaciology*, 56(198), 723-734. doi:10.3189/002214310793146313

Amundson JM, Truffer M, Lüthi MP, Fahnestock M, West M and Motyka RJ (2008) Glacier, fjord, and seismic response to recent large calving events, Jakobshavn Isbræ, Greenland. *Geophysical Research Letters*, 35(22). doi:10.1029/2008GL035281

Aschwanden A and 7 others (2019) Contribution of the Greenland Ice Sheet to sea level over the next millennium. *Science advances*, 5(6), eaav9396. doi:10.1126/sciadv.aav9396

Åström JA and 10 others (2014) Termini of calving glaciers as self-organized critical systems. *Nature Geoscience*, 7(12), 874-878. doi:10.1038/ngeo2290

Bamber JL, Westaway RM, Marzeion B and Wouters B (2018) The land ice contribution to sea level during the satellite era. *Environmental Research Letters*, 13(6), 063008. doi:10.1088/1748-9326/aac2f0

Bao W and Moffat C (2024) Impact of shallow sills on circulation regimes and submarine melting in glacial fjords. *The Cryosphere*, 18(1), 187-203. doi:10.5194/tc-18-187-2024

Bartholomaus TC, Larsen CF, West ME, O'Neel S, Pettit EC and Truffer M (2015) Tidal and seasonal variations in calving flux observed with passive seismology. *Journal of Geophysical Research: Earth Surface*, 120(11), 2318-2337.

doi:10.1002/2015JF003641

Baurley NR, Tomsett C and Hart JK (2022) Assessing UAV-based laser scanning for monitoring glacial processes and interactions at high spatial and temporal resolutions. *Frontiers in Remote Sensing*, 3, 1027065. doi:10.3389/frsen.2022.1027065 Benn D and Evans DJ (2010) Glaciers and glaciation, 2nd edition. *Routledge*, London. doi:10.4324/9780203785010 Benn DI, Warren CR and Mottram RH (2007) Calving processes and the dynamics of calving glaciers. *Earth-Science Reviews*, 82(3-4), 143-179. doi:10.1016/j.earscirev.2007.02.002

Bintanja R and Van der Linden EC (2013) The changing seasonal climate in the Arctic. *Scientific reports*, 3(1), 1-8. doi:10.1038/srep01556

Błaszczyk M and 7 others (2024) High temporal resolution records of the velocity of Hansbreen, a tidewater glacier in Svalbard. *Earth System Science Data*, 16(4), 1847-1860. doi:10.5194/essd-16-1847-2024

Błaszczyk M and 10 others (2021) Factors controlling terminus position of Hansbreen, a tidewater glacier in Svalbard. *Journal of Geophysical Research: Earth Surface*, 126(2), e2020JF005763 (doi:10.1029/2020JF005763)

Błaszczyk M and 7 others (2019) Freshwater input to the Arctic fjord Hornsund (Svalbard). *Polar Research*. doi:10.33265/polar.v38.3506

Błaszczyk M, Jania JA and Hagen JO (2009) Tidewater glaciers of Svalbard: Recent changes and estimates of calving fluxes. *Polish Polar Research*, (2)

Brown CS, Meier MF and Post A (1982) Calving speed of Alaska tidewater glaciers, with application to Columbia Glacier. *USGS Prof. Pap.* 1258-C, C1-C13. US Government Printing Office, Washington.

Bruzzone G, Odetti A, Caccia M and Ferretti R (2020) Monitoring of sea-ice-atmosphere interface in the proximity of Arctic tidewater glaciers: The contribution of marine robotics. *Remote Sensing*, 12(11), 1707. doi:10.3390/rs12111707

Carroll D, Sutherland DA, Shroyer EL, Nash JD, Catania GA and Stearns LA (2017) Subglacial discharge-driven renewal of tidewater glacier fjords. *Journal of Geophysical Research: Oceans*, 122(8), 6611-6629. doi:10.1002/2017JC012962

Carroll D, Sutherland DA, Shroyer EL, Nash JD, Catania GA and Stearns LA (2015) Modeling turbulent subglacial meltwater plumes: Implications for fjord-scale buoyancy-driven circulation. *Journal of Physical Oceanography*, 45(8), 2169-2185. doi:10.1175/JPO-D-15-0033.1

Cheng L and 10 others (2022) Another record: ocean warming continues through 2021 despite La Niña conditions. *Advances in Atmospheric Sciences*, 39(3), 373-385. doi:10.1007/s00376-022-1461-3

Chu VW, Smith LC, Rennermalm AK, Forster RR, Box JE and Reeh N (2009) Sediment plume response to surface melting and supraglacial lake drainages on the Greenland ice sheet. *Journal of Glaciology*, 55(194), 1072-1082. doi:10.3189/002214309790794904

Ciepły M and 6 others (2023). Seasonal changes in submarine melting mechanisms controlling frontal ablation of Hansbreen, Svalbard. *Journal of Glaciology*, 69(278), 1886-1899. doi:10.1017/jog.2023.69

Cook SJ, Christoffersen P, Truffer M, Chudley TR and Abellan A (2021) Calving of a large Greenlandic tidewater glacier has complex links to meltwater plumes and mélange. *Journal of Geophysical Research: Earth Surface*, 126(4), e2020JF006051. doi:10.1029/2020JF006051

Cowton TR, Sole AJ, Nienow PW, Slater DA and Christoffersen P (2018) Linear response of east Greenland's tidewater glaciers to ocean/atmosphere warming. *Proceedings of the National Academy of Sciences*, 115(31), 7907-7912.

doi:10.1073/pnas.1801769115

Cowton T, Slater D, Sole A, Goldberg D and Nienow P (2015) Modeling the impact of glacial runoff on fjord circulation and submarine melt rate using a new subgrid-scale parameterization for glacial plumes. *Journal of Geophysical Research:*Oceans, 120(2), 796-812. doi:10.1002/2014JC010324

Downs J, Brinkerhoff D and Morlighem M (2023). Inferring time-dependent calving dynamics at Helheim Glacier. *Journal of Glaciology*, 69(274):381-396. doi:10.1017/jog.2022.68

Everett A, Murray T, Selmes N, Holland D and Reeve DE (2021) The impacts of a subglacial discharge plume on calving, submarine melting, and mélange mass loss at Helheim Glacier, South East Greenland. *Journal of Geophysical Research: Earth Surface*, 126(3), e2020JF005910. doi:10.1029/2020JF005910

Fürst JJ, Goelzer H and Huybrechts P (2015) Ice-dynamic projections of the Greenland ice sheet in response to atmospheric and oceanic warming. *The Cryosphere*, 9(3), 1039-1062. doi:10.5194/tc-9-1039-2015

Glowacki O (2022) Distinguishing subaerial and submarine calving with underwater noise. *Journal of Glaciology*, 68(272), 1185-1196. doi:10.1017/jog.2022.32

Glowacki O and Deane GB (2020) Quantifying iceberg calving fluxes with underwater noise. *The Cryosphere*, 14(3), 1025-1042. doi:10.5194/tc-14-1025-2020

Glowacki O, Deane GB, Moskalik M, Blondel P, Tegowski J and Blaszczyk M (2015) Underwater acoustic signatures of glacier calving. *Geophysical Research Letters*, 42(3), 804-812. doi:10.1002/2014GL062859

Grabiec M, Jania JA, Puczko D, Kolondra L and Budzik TS (2012) Surface and bed morphology of Hansbreen, a tidewater glacier in Spitsbergen. *Polish Polar Research*, 33(2). doi:10.2478/v10183-012-0010-7

Greene CA, Gardner AS, Schlegel NJ and Fraser AD (2022) Antarctic calving loss rivals ice-shelf thinning. *Nature*, 609(7929), 948-953. doi:10.1038/s41586-022-05037-w

Hagen JO, Kohler J, Melvold K and Winther JG (2003) Glaciers in Svalbard: mass balance, runoff and freshwater flux. *Polar Research*, 22(2), 145-159. doi:10.1111/j.1751-8369.2003.tb00104.x

Harrison WD, Echelmeyer KA, Cosgrove DM and Raymond CF (1992) The determination of glacier speed by time-lapse photography under unfavorable conditions. *Journal of Glaciology*, 38(129), 257-265. doi:10.3189/S002214300000366X Holland DM, Thomas RH, De Young B, Ribergaard MH and Lyberth B (2008) Acceleration of Jakobshavn Isbræ triggered by warm subsurface ocean waters. *Nature geoscience*, 1(10), 659-664. doi: 10.1038/ngeo316

Holmes FA, van Dongen E, Noormets R, Pętlicki M and Kirchner N (2023) Impact of tides on calving patterns at Kronebreen, Svalbard–insights from three-dimensional ice dynamical modelling. *The Cryosphere*, 17(5), 1853-1872. doi:10.5194/tc-17-1853-2023

Holmes FA, Kirchner N, Kuttenkeuler J, Krützfeldt J and Noormets R. (2019) Relating ocean temperatures to frontal ablation rates at Svalbard tidewater glaciers: Insights from glacier proximal datasets. *Scientific reports*, 9(1), 9442. doi:10.1038/s41598-019-45077-3

How P and 8 others (2019) Calving controlled by melt-under-cutting: detailed calving styles revealed through time-lapse observations. *Annals of Glaciology*, 60(78), 20-31. doi:10.1017/aog.2018.28

Howe and 7 others (2019) Autonomous underwater vehicle (AUV) observations of recent tidewater glacier retreat, western Svalbard. *Marine Geology*, 417, 106009. doi:10.1016/j.margeo.2019.106009

Igneczi A and Bamber JL (2024) A high-resolution pan-Arctic meltwater discharge dataset from 1950 to 2021. *Earth System Science Data Discussions*, 2024, 1-24. doi:10.5194/essd-2024-169

Jackson RH and 8 others (2017) Near-glacier surveying of a subglacial discharge plume: Implications for plume parameterizations. *Geophysical Research Letters*, 44(13), 6886-6894. doi:10.1002/2017GL073602

Jania J (1988) Dynamiczne procesy glacjalne na południowym Spitsbergenie (w świetle badań fotointerpretacyjnych I fotogrametrycznych) [Dynamic glacial processes in south Spitsbergen (in the light of photointerpretation and photogrammetric research)]. *Prace Naukowe Uniwersytetu Śląskiego w Katowicach* No. 955: Katowice (in Polish).

Jania J and Kolondra LJ (1982) Field investigations performed during the glaciological Spitsbergen expedition in the summer of 1982: *interim report*. Katowice, University of Silesia. Faculty of Earth Sciences, Department of Geomorphology.

Jain V, Korhonen M, Głowacki O and Moskalik M (2024) Hydrography of the inner basins in Hornsund (Svalbard): heat advection near tidewater glaciers. *Journal of Geophysical Research: Oceans*, 129(11), e2024JC021273.

doi:10.1029/2024JC021273

Johnson GC and 10 others (2021) Global oceans. *Bulletin of the American Meteorological Society*, 102(8), S143-S198. doi:10.1175/BAMS-D-21-0083.1

Joughin I, Abdalati W and Fahnestock M (2004) Large fluctuations in speed on Greenland's Jakobshavn Isbrae glacier. *Nature* 432, 608–610. doi:10.1038/nature03130

Joughin I, Tulaczyk S, Fahnestock M and Kwok R (1996) A mini-surge on the Ryder Glacier, Greenland, observed by satellite radar interferometry. *Science*, 274(5285), 228-230. doi:10.1126/science.274.5285.228

Kamb B, Engelhardt H, Fahnestock MA, Humphrey N, Meier M and Stone D (1994) Mechanical and hydrologic basis for the rapid motion of a large tidewater glacier: 2. Interpretation. *Journal of Geophysical Research: Solid Earth*, 99(B8), 15231-15244. doi:10.1029/94JB00467

King MD and 8 others (2020) Dynamic ice loss from the Greenland Ice Sheet driven by sustained glacier retreat. *Communications Earth & Environment*, 1(1), p.1. doi:10.1038/s43247-020-0001-2

Kneib-Walter A, Lüthi MP, Moreau L and Vieli A (2021) Drivers of recurring seasonal cycle of glacier calving styles and patterns. *Frontiers in Earth Science*, 9, 667717. doi:10.1002/2015RG000494

Kochtitzky W and Copland L (2022) Retreat of Northern Hemisphere marine-terminating glaciers, 2000–2020. *Geophysical Research Letters*, 49(3), e2021GL096501. doi:10.1029/2021GL096501

Korhonen M, Moskalik M, Głowacki O and Jain V (2024) Oceanographic monitoring in Hornsund fjord, Svalbard. *Earth System Science Data*, 16(10), 4511-4527. doi:10.5194/essd-16-4511-2024

Krabill W and 8 others (1999) Rapid thinning of parts of the southern Greenland ice sheet. *Science*, 283(5407), 1522-1524. doi:10.1126/science.283.5407.1522

Kristensen L and Benn D (2012) A surge of the glaciers Skobreen–Paulabreen, Svalbard, observed by time-lapse photographs and remote sensing data. *Polar Research*, 31(1), p.11106. doi:10.3402/polar.v31i0.11106

Li T, Heidler K, Mou L, Ignéczi Á, Zhu XX and Bamber JL (2023) A high-resolution calving front data product for marine-terminating glaciers in Svalbard. *Earth System Science Data Discussions*, 2023, 1-28. doi:10.5194/essd-16-919-2024

Luckman A, Benn DI, Cottier F, Bevan S, Nilsen F and Inall M (2015) Calving rates at tidewater glaciers vary strongly with ocean temperature. *Nature communications*, 6(1), 8566. doi:10.1038/ncomms9566

Lüthi MP and Vieli A (2016) Multi-method observation and analysis of a tsunami caused by glacier calving. *The Cryosphere*, 10(3), 995-1002. doi:10.5194/tc-10-995-2016

Ma J, Zhou J, Göttsche FM, Liang S, Wang S and Li M (2020) A global long-term (1981–2000) land surface temperature product for NOAA AVHRR. *Earth System Science Data*, 12(4), 3247-3268. doi:10.5194/essd-12-3247-2020

Mankoff KD, Straneo F, Cenedese C, Das SB, Richards CG and Singh H (2016) Structure and dynamics of a subglacial discharge plume in a Greenlandic fjord. *Journal of Geophysical Research: Oceans*, 121(12), 8670-8688. doi:10.1002/2016JC011764

Marzeion B and 10 others (2020) Partitioning the uncertainty of ensemble projections of global glacier mass change. *Earth's Future*, 8(7), e2019EF001470. doi:10.1029/2019EF001470

Meier MF and Post A (1987) Fast tidewater glaciers. *Journal of Geophysical Research: Solid Earth*, 92(B9), 9051-9058. doi:10.1029/JB092iB09p09051

Meier MF, Rasmussen LA, Krimmel RM, Olsen RW and Frank D (1985) Photogrammetric determination of surface altitude, terminus position, and ice velocity of Columbia Glacier, Alaska. *USGS Prof. Pap.* 1258-F. US Government Printing Office, Washington.

Meredith and 10 others (2022) Internal tsunami genesis and ocean mixing driven by glacier calving in Antarctica. *Science advances*, 8(47), eadd0720. doi:10.1126/sciadv.add0720

Minowa M, Schaefer M, Sugiyama S, Sakakibara D and Skvarca P (2021) Frontal ablation and mass loss of the Patagonian icefields. *Earth and Planetary Science Letters*, 561, 116811. doi:10.1016/j.epsl.2021.116811

Minowa M and 7 others (2019) Calving flux estimation from tsunami waves. *Earth and Planetary Science Letters*, 515, 283-290. doi:10.1016/j.epsl.2019.03.023

Minowa M, Podolskiy EA, Sugiyama S, Sakakibara D and Skvarca P (2018) Glacier calving observed with time-lapse imagery and tsunami waves at Glaciar Perito Moreno, Patagonia. *Journal of Glaciology*, 64(245), 362-376. doi:10.1017/jog.2018.28 Motyka RJ, Dryer WP, Amundson J, Truffer M and Fahnestock M (2013) Rapid submarine melting driven by subglacial

discharge, LeConte Glacier, Alaska. *Geophysical Research Letters*, 40(19), 5153-5158. doi:10.1002/grl.51011

Motyka RJ, Hunter L, Echelmeyer KA and Connor C (2003) Submarine melting at the terminus of a temperate tidewater glacier, LeConte Glacier, Alaska, USA. *Annals of Glaciology*, 36, 57-65. doi:10.3189/172756403781816374

Mouginot J and 8 others (2019). Forty-six years of Greenland Ice Sheet mass balance from 1972 to 2018. *Proceedings of the national academy of sciences*, 116(19), 9239-9244. doi:10.1073/pnas.1904242116

Mukherji A (2023) Climate change 2023 synthesis report. doi:10.59327/ipcc/ar6-9789291691647.001

Murray T, and 9 others (2015) Dynamics of glacier calving at the ungrounded margin of Helheim Glacier, southeast

Greenland. Journal of Geophysical Research: Earth Surface, 120(6), 964-982. doi:10.1002/2015JF003531

Nick FM and 7 others (2013) Future sea-level rise from Greenland's main outlet glaciers in a warming climate. *Nature*, 497(7448), 235-238. doi:10.1038/nature12068

Nick FM, Vieli A, Howat IM, and Joughin I (2009) Large-scale changes in Greenland outlet glacier dynamics triggered at the terminus. *Nat. Geosci*, 2, 110–114. doi:10.1038/ngeo394

Nuth C and 7 others (2013) Decadal changes from a multi-temporal glacier inventory of Svalbard. *The Cryosphere*, 7(5), 1603-1621. doi:10.5194/tc-7-1603-2013

Nye JF (1952) The mechanics of glacier flow. Journal of Glaciology, 2(12), 82-93. doi:10.3189/S0022143000033967

O'Neel S, Marshall HP, McNamara DE and Pfeffer WT (2007) Seismic detection and analysis of icequakes at Columbia Glacier, Alaska. *Journal of Geophysical Research: Earth Surface*, 112(F3). doi:10.1029/2006JF000595

O'Neel S, Pfeffer WT, Krimmel R and Meier M (2005) Evolving force balance at Columbia Glacier, Alaska, during its rapid retreat. *Journal of Geophysical Research: Earth Surface*, 110(F3). doi:10.1029/2005JF000292

O'Neel S, Echelmeyer KA and Motyka RJ (2003) Short-term variations in calving of a tidewater glacier: LeConte Glacier, Alaska, USA. *Journal of Glaciology*, 49(167), 587-598. doi:10.3189/172756503781830430

Oceans G (2021) State of the climate in 2020. State of the climate in 2020, 102(8), 142. doi:10.1175/BAMS-D-21-0083.1

Osika A and Jania J (2024) Geomorphological and historical records of the surge-type behaviour of Hansbreen (Svalbard). *Annals of Glaciology*, 65, e31. doi:10.1017/aog.2024.32

Osuch M and Wawrzyniak T (2016) Climate projections in the Hornsund area, Southern Spitsbergen. *Polish Polar Research*, 37(3), 379-402. doi:10.1515/popore-2016-0020

Pelto MS and Warren CR (1991) Relationship between tidewater glacier calving velocity and water depth at the calving front. *Annals of glaciology*, 15, 115-118. doi:10.3189/S0260305500009617

Pętlicki M and Kinnard C (2016) Calving of Fuerza Aérea Glacier (Greenwich Island, Antarctica) observed with terrestrial laser scanning and continuous video monitoring. *Journal of Glaciology*, 62(235), 835-846. doi:10.1017/jog.2016.72

Pętlicki M, Ciepły M, Jania JA, Promińska A and Kinnard C (2015) Calving of a tidewater glacier driven by melting at the waterline. *Journal of Glaciology*, 61(229), 851-863. doi:10.3189/2015JoG15J062

Pettit EC (2012) Passive underwater acoustic evolution of a calving event. *Annals of Glaciology*, 53(60), 113-122. doi:10.3189/2012AoG60A137

Podgorski J, Pętlicki M and Kinnard C (2018) Revealing recent calving activity of a tidewater glacier with terrestrial LiDAR reflection intensity. *Cold Regions Science and Technology*, 151, 288-301. doi:10.1016/j.coldregions.2018.03.003

Podolskiy EA, Murai Y, Kanna N and Sugiyama S (2022) Glacial earthquake-generating iceberg calving in a narwhal summering ground: The loudest underwater sound in the Arctic?. *The Journal of the Acoustical Society of America*, 151(1), 6-16. doi:10.1121/10.0009166

Podolskiy EA and Walter F (2016) Cryoseismology. *Reviews of geophysics*, 54(4), 708-758. doi: 10.1002/2016RG000526 Promińska A, Falck E and Walczowski W (2018) Interannual variability in hydrography and water mass distribution in Hornsund, an Arctic fjord in Syalbard. Polar Research, 37(1), 1495546. doi:10.1080/17518369.2018.1495546

Promińska A, Cisek M and Walczowski W (2017) Kongsfjorden and Hornsund hydrography–comparative study based on a multiyear survey in fjords of west Spitsbergen. *Oceanologia*, 59(4), 397-412. doi:10.1016/j.oceano.2017.07.003

Rantanen M and 7 others (2022) The Arctic has warmed nearly four times faster than the globe since 1979. *Communications earth & environment*, 3(1), 168. doi:10.1038/s43247-022-00498-3

Reese R and 10 others (2022) The stability of present-day Antarctic grounding lines—Part B: Possible commitment of regional collapse under current climate. *The Cryosphere Discussions*, 2022, 1-33. doi:10.5194/tc-17-3761-2023

RGI Consortium (2017) Randolph glacier inventory - A dataset of global glacier outlines, Version 6.0, GLIMS. doi:10.7265/4m1f-gd79

Richardson JP, Waite GP, FitzGerald KA and Pennington WD (2010) Characteristics of seismic and acoustic signals produced by calving, Bering Glacier, Alaska. *Geophysical Research Letters*, 37(3). doi:10.1029/2009GL041113

Rignot E, Mouginot J, Scheuchl B, Van Den Broeke M, Van Wessem MJ and Morlighem M (2019) Four decades of Antarctic Ice Sheet mass balance from 1979–2017. *Proceedings of the National Academy of Sciences*, 116(4), 1095-1103. doi:10.1073/pnas.1812883116

Rignot E, Fenty I, Xu Y, Cai C and Kemp C (2015) Undercutting of marine-terminating glaciers in West Greenland. *Geophysical Research Letters*, 42(14), 5909-5917. doi:10.1002/2015GL064236

Rignot E, Koppes M and Velicogna I (2010) Rapid submarine melting of the calving faces of West Greenland glaciers. *Nature Geoscience*, 3(3), 187-191. doi:10.1038/ngeo765

Robel AA, Roe GH and Haseloff M (2018) Response of marine-terminating glaciers to forcing: time scales, sensitivities, instabilities, and stochastic dynamics. *Journal of Geophysical Research: Earth Surface*, 123(9), 2205-2227. doi:10.1029/2018JF004709

Ryan JC and 7 others (2015) UAV photogrammetry and structure from motion to assess calving dynamics at Store Glacier, a large outlet draining the Greenland ice sheet. *The Cryosphere*, 9(1), 1-11. doi:10.5194/tc-9-1-2015

Scambos TA, Hulbe C, Fahnestock M and Bohlander J (2000) The link between climate warming and break-up of ice shelves in the Antarctic Peninsula. *Journal of Glaciology*, 46(154), 516-530. doi:10.3189/172756500781833043

Schauer U, Fahrbach E, Osterhus S and Rohardt G (2004) Arctic warming through the Fram Strait: Oceanic heat transport from 3 years of measurements. *Journal of Geophysical Research: Oceans*, 109(C6). doi:10.1029/2003JC001823

Schild KM and 9 others (2018) Glacier calving rates due to subglacial discharge, fjord circulation, and free convection. *Journal of Geophysical Research: Earth Surface*, 123(9), 2189-2204. doi:10.1029/2017JF004520

Schmidt LS, Schuler TV, Thomas EE and Westermann S (2023) Meltwater runoff and glacier mass balance in the high Arctic: 1991–2022 simulations for Svalbard. *The Cryosphere*, 17(7), 2941-2963. doi:10.5194/tc-17-2941-2023

Schuler TV and 10 others (2020) Reconciling Svalbard glacier mass balance. *Frontiers in Earth Science*, 8, 156. doi:10.3389/feart.2020.00156

Serreze MC and Barry RG (2011) Processes and impacts of Arctic amplification: A research synthesis. *Global and planetary change*, 77(1-2), 85-96. doi:10.1016/j.gloplacha.2011.03.004

Sikonia WG (1982) Finite element glacier dynamics model applied to Columbia Glacier, Alaska. *USGS Prof. Pap.* 1258-B, 7 4 p. US Government Printing Office, Washington.

Slater DA and Straneo F (2022) Submarine melting of glaciers in Greenland amplified by atmospheric warming. *Nature Geoscience*, 15(10), 794-799. doi:10.1038/s41561-022-01035-9

Sohn HG, Jezek KC and van der Veen CJ (1998) Jakobshavn Glacier, West Greenland: 30 years of spaceborne observations. *Geophysical Research Letters*, 25(14), 2699-2702. doi:10.1029/98GL01973

Straneo F and Cenedese C (2015) The dynamics of Greenland's glacial fjords and their role in climate. *Annual review of marine science*, 7(1), 89-112. doi:10.1146/annurev-marine-010213-135133

Straneo F and 10 others (2013) Challenges to understanding the dynamic response of Greenland's marine terminating glaciers to oceanic and atmospheric forcing. *Bulletin of the American Meteorological Society*, 94(8), 1131-1144. doi:10.1175/BAMS-D-12-00100.1

Strzelewicz A, Przyborska A and Walczowski W (2022) Increased presence of Atlantic Water on the shelf south-west of Spitsbergen with implications for the Arctic fjord Hornsund. *Progress in Oceanography*, 200, 102714. doi:10.1016/j.pocean.2021.102714

Sutherland DA and 8 others (2019) Direct observations of submarine melt and subsurface geometry at a tidewater glacier. *Science*, 365(6451), 369-374. doi:10.1126/science.aax3528

Swirad ZM, Johansson AM and Malnes E (2024) Extent, duration and timing of the sea ice cover in Hornsund, Svalbard, from 2014–2023. *The Cryosphere*, 18(2), 895-910. doi:10.5194/egusphere-2023-2592

Swirad ZM, Moskalik M and Herman A (2023) Wind wave and water level dataset for Hornsund, Svalbard (2013–2021). *Earth System Science Data Discussions*, 2023, 1-15. doi:10.5194/essd-15-2623-2023

The IMBIE Team (2020) Mass balance of the Greenland Ice Sheet from 1992 to 2018. *Nature*, 579, 233–239. doi:10.1038/s41586-019-1855-2

Truffer M and Motyka RJ (2016) Where glaciers meet water: Subaqueous melt and its relevance to glaciers in various settings. *Reviews of Geophysics*, 54(1), 220-239. doi:10.1002/2015RG000494

Vallot D and 6 others (2019) Automatic detection of calving events from time-lapse imagery at Tunabreen,

Svalbard. Geoscientific Instrumentation, Methods and Data Systems, 8(1), 113-127. doi:10.5194/gi-8-113-2019

Vallot D and 9 others (2017) Basal dynamics of Kronebreen, a fast-flowing tidewater glacier in Svalbard: non-local spatio-temporal response to water input. *Journal of Glaciology*, 63(242), 1012-1024. doi:10.1017/jog.2017.69

Van den Broeke MR and 7 others (2016) On the recent contribution of the Greenland ice sheet to sea level change. *The Cryosphere*, 10(5), 1933-1946. doi:10.5194/tc-10-1933-2016

Van der Veen CJ (1998) Fracture mechanics approach to penetration of surface crevasses on glaciers. *Cold Regions Science and Technology*, 27(1), 31-47. doi:10.1016/S0165-232X(98)00006-8

Van Der Veen CJ (1996) Tidewater calving, *Journal of Glaciology*, 42(141), 375–385. doi:10.3189/S0022143000004226 Van Pelt W and 10 others (2019) A long-term dataset of climatic mass balance, snow conditions, and runoff in Svalbard (1957–2018). *The Cryosphere*, 13(9), 2259-2280. doi:10.5194/tc-13-2259-2019

Venteris ER (1999) Rapid tidewater glacier retreat: a comparison between Columbia Glacier, Alaska and Patagonian calving glaciers. *Global and Planetary Change*, 22(1-4), 131-138. doi:10.1016/S0921-8181(99)00031-4

Vieli A, Jania J, Blatter H and Funk M (2004) Short-term velocity variations on Hansbreen, a tidewater glacier in Spitsbergen. *Journal of Glaciology*, 50(170), 389-398. doi:10.3189/172756504781829963

Vieli A, Jania J and Kolondra L (2002) The retreat of a tidewater glacier: observations and model calculations on Hansbreen, Spitsbergen, *Journal of Glaciology*, 48(163), 592–600. doi:10.3189/172756502781831089

Vieli A, Funk M and Blatter H (2000) Tidewater glaciers: frontal flow acceleration and basal sliding, *Annals of Glaciology*, 31, 217–221. doi:10.3189/172756400781820417

Wagner TJ and 6 others (2019) Large spatial variations in the flux balance along the front of a Greenland tidewater glacier. *The Cryosphere*, 13(3), 911-925. doi:10.5194/tc-13-911-2019

Walter F, O'Neel S, McNamara D, Pfeffer WT, Bassis JN and Fricker HA (2010) Iceberg calving during transition from grounded to floating ice: Columbia Glacier, Alaska. *Geophysical Research Letters*, 37(15). doi:10.1029/2010GL043201

Wawrzyniak T and Osuch M (2020) A 40-year High Arctic climatological dataset of the Polish Polar Station Hornsund (SW Spitsbergen, Svalbard). *Earth System Science Data*, 12(2), 805-815. doi:10.5194/essd-12-805-2020

Weertman J (1957) On the Sliding of Glaciers, Journal of Glaciology, 3(21), 33-38. doi:10.3189/S0022143000024709

Wehrlé A, Lüthi MP, Walter A, Jouvet G, and Vieli A (2021) Automated detection and analysis of surface calving waves with a terrestrial radar interferometer at the front of Eqip Sermia, Greenland. *The Cryosphere*, 15, 5659–5674. doi: 10.5194/tc-15-5659-2021

Weidner E and 9 others (2024) High frequency broadband acoustic systems as a tool for high latitude glacial fjord research. *EGUsphere*, 2024, 1-41. doi:10.5194/egusphere-2024-3025

Welty EZ, Bartholomaus TC, O'Neel S and Pfeffer WT (2013) Cameras as clocks. *Journal of Glaciology*, 59(214), 275-286. doi:10.3189/2013JoG12J126

Westoby MJ, Brasington J, Glasser NF, Hambrey MJ and Reynolds JM (2012) Structure-from-Motion Photogrammetry: A low-cost, effective tool for geoscience applications. *Geomorphology*, 179, 300-314. doi:10.1016/j.geomorph.2012.08.021

Winberry JP, Huerta AD, Anandakrishnan S, Aster RC, Nyblade AA and Wiens DA (2020) Glacial earthquakes and precursory seismicity associated with Thwaites Glacier calving. *Geophysical Research Letters*, 47(3), e2019GL086178.

Wood M and 10 others (2021) Ocean forcing drives glacier retreat in Greenland. *Science advances*, 7(1), eaba7282. doi:10.1126/sciadv.aba7282

Zemp M and 10 others (2019) Global glacier mass changes and their contributions to sea-level rise from 1961 to 2016. *Nature*, 568(7752), 382-386. doi:10.1038/s41586-019-1071-0

doi:10.1029/2019GL086178

LIST OF FIGURE CAPTIONS

Fig. 1. A map of the study site. The inset map (top right) shows the location of Svalbard, with star indicating Hornsund Fjord, where Hansbreen is situated. Color dots show positions of the camera (yellow, 'TLC'), CTD casts (pink, 'CTD'), moorings with the pressure (red, 'P') and temperature (pink, 'T') sensors, and the Polish Polar Station Hornsund (green, 'PPS'). Red lines show division of the terminus into five zones (I-V). Sentinel-2 true color satellite image from July 30, 2016 provided by the Sentinel Hub. Bathymetric data from Błaszczyk and others (2020). Coordinates are given in UTM zone 33N (m).

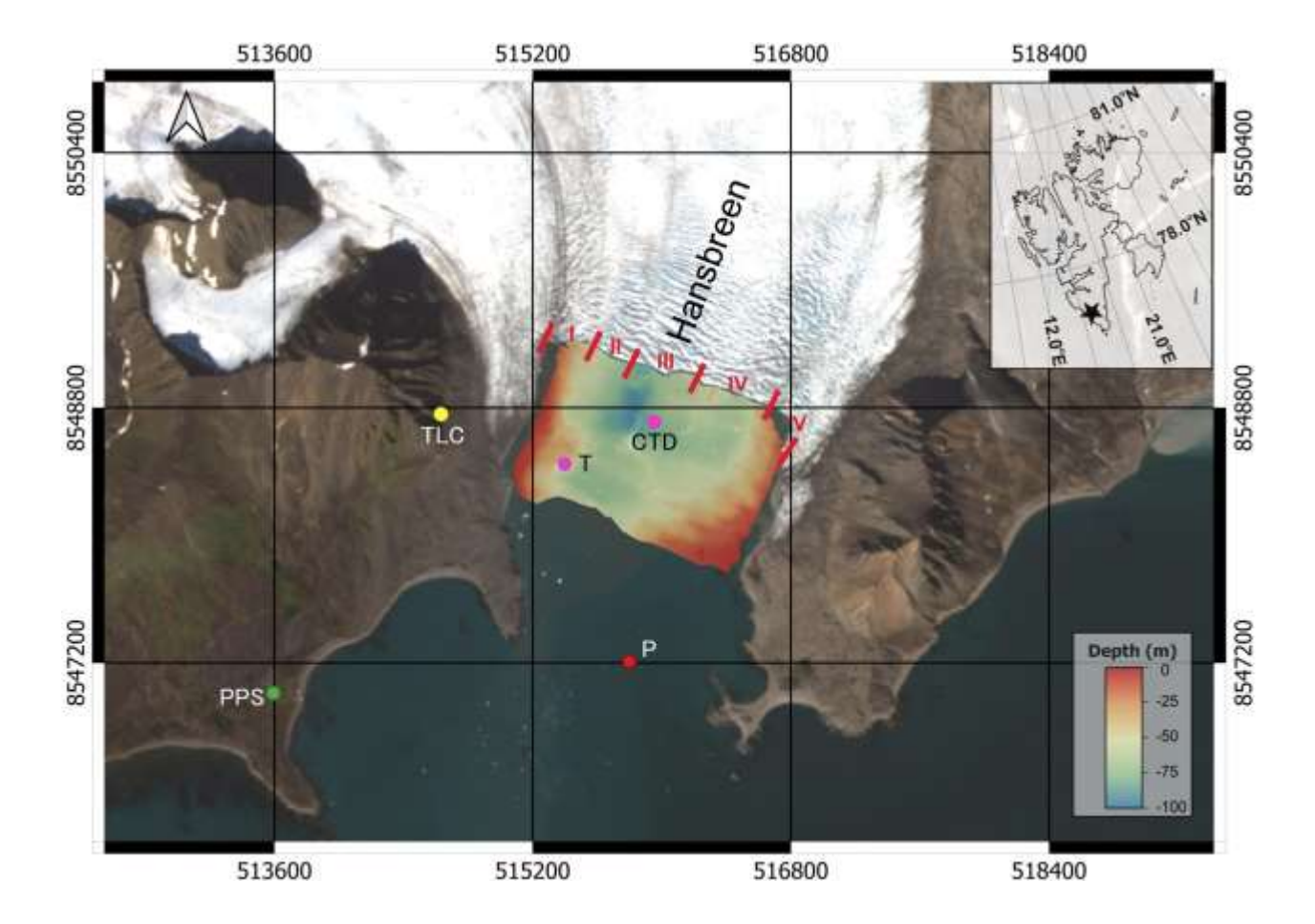


Fig. 2. Methodology of the image analysis. (a) Division of the glacier terminus into five zones (ZI to ZV). (b) Classification of calving events into four size categories, defined as fraction of the glacier terminus height: size 1 (<25 %), size 2 (25–50 %), size 3 (50–75 %), and size 4 (>75 %). (c-f) Examples of different calving styles. Each pair of image is separated by 15 minutes; the second image in each pair includes a yellow outline marking the calved portion of the terminus, highlighting the visual differences used to classify events.

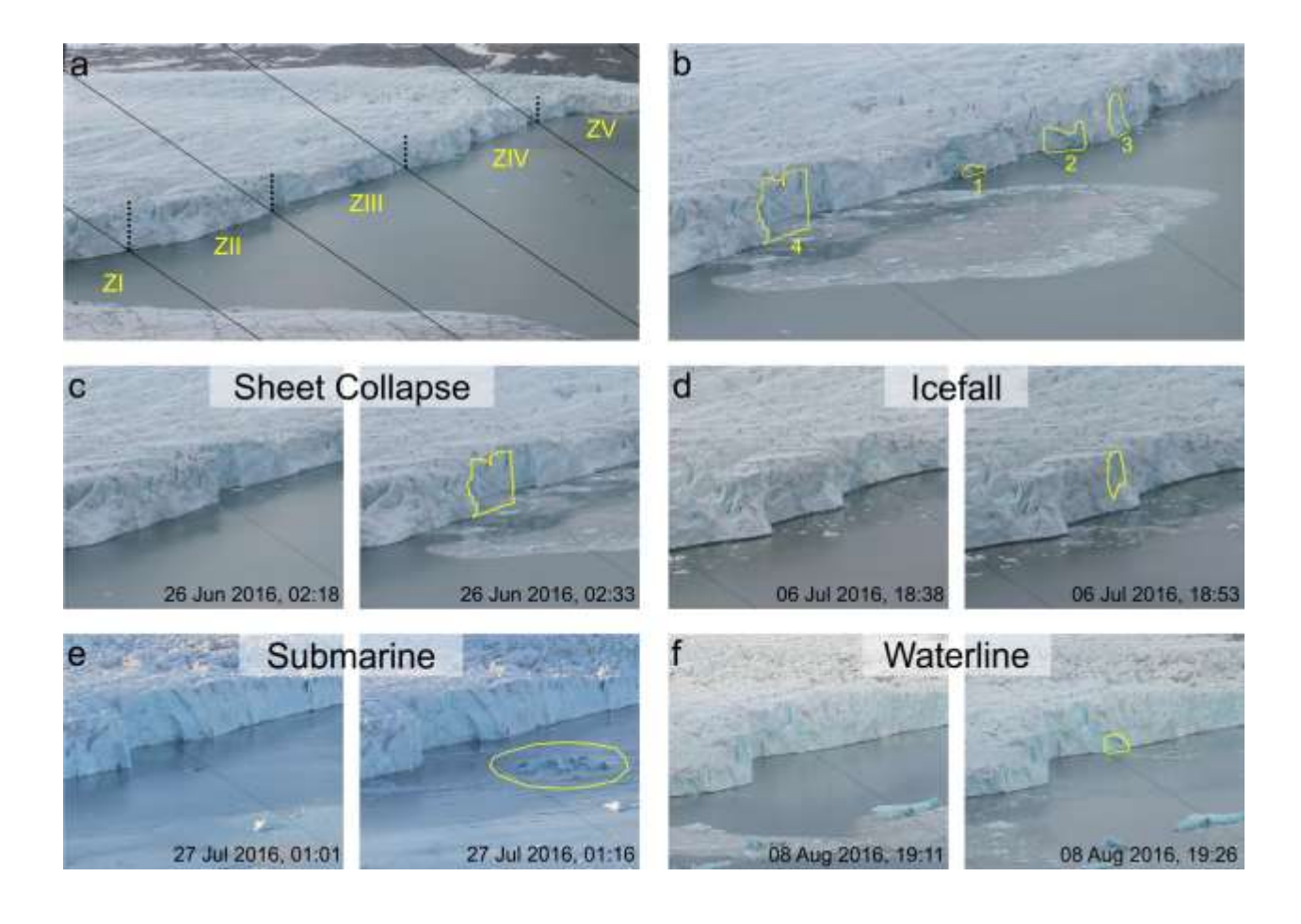


Fig. 3. Calving frequency and environmental parameters at Hansbreen over a six-month period (May-Oct 2016). (a) Total calving frequency at a daily scale (orange dots) and averaged over a five-day period (orange line), and the corresponding ocean temperatures measured at the mooring position and during the CTD casts. Median values of ocean temperature from the CTD casts are marked with magenta dots (for full water column), and standard deviations from the mean are indicated by whiskers (b) Calving frequency for different event sizes and cumulative event size per day (black line). (c) Daily air temperature and precipitation, and the modelled meltwater runoff.

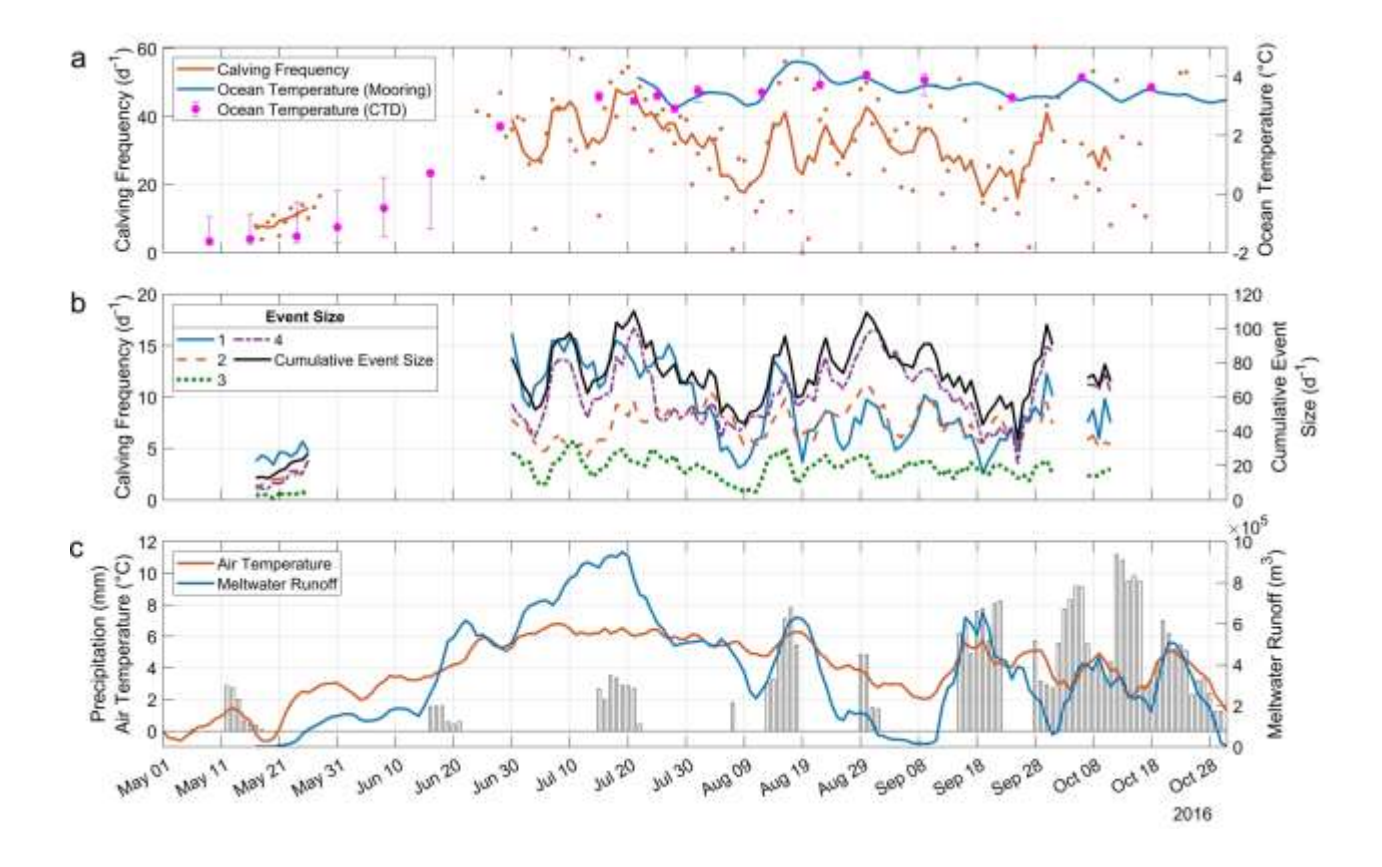


Fig. 4. Spatio-temporal variability of calving frequency in different zones at Hansbreen from May to October, 2016. (a) Calving frequency averaged over a five-day period in different zones. (b) Monthly calving frequency values in each zone normalized by variable terminus width (bars), and monthly image coverage (black circles).

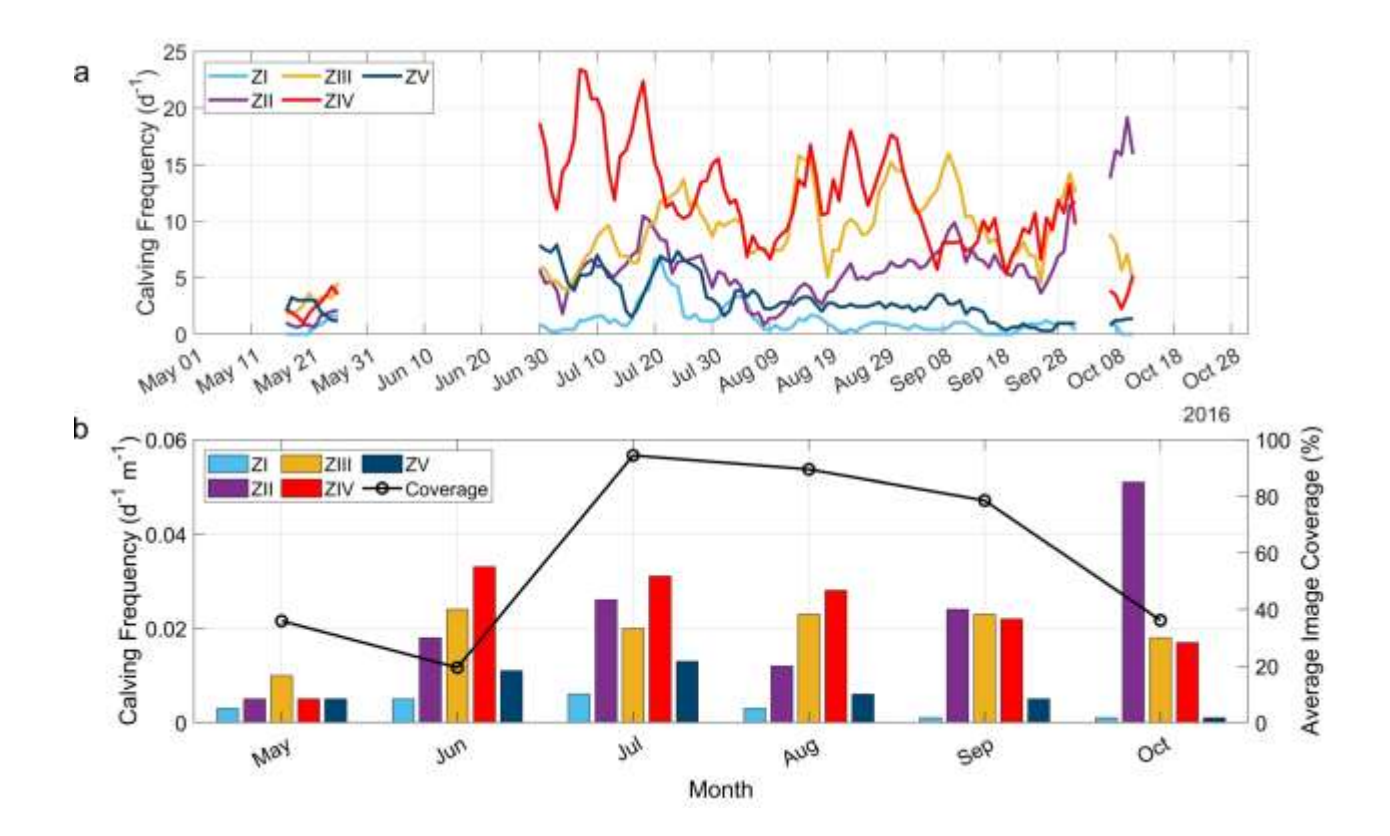


Fig. 5. Spatio-temporal variability of calving frequency for different styles at Hansbreen from May to October, 2016 (a) Calving frequency averaged over a five-day period for different styles. (b) Percentage distribution of calving styles in all zones (ZI-ZV).

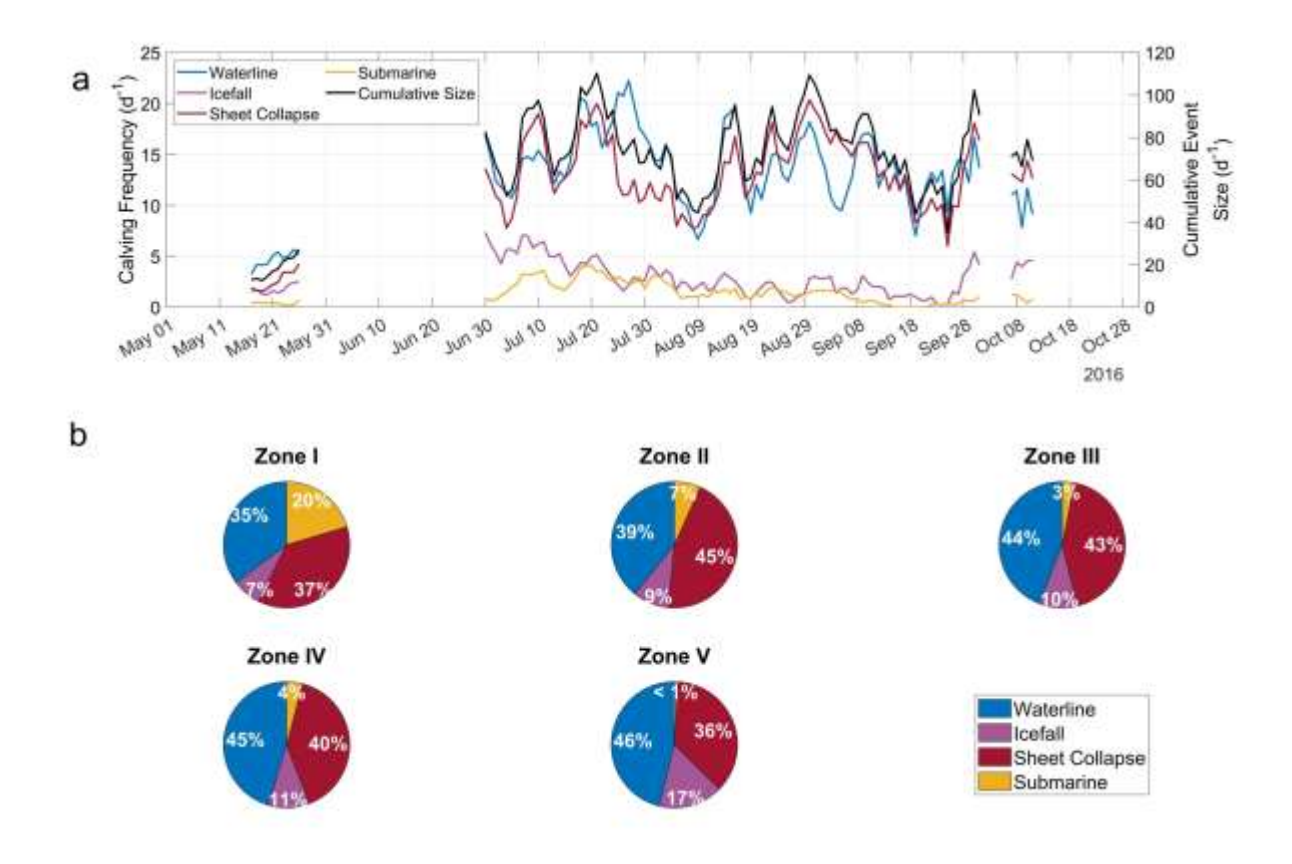
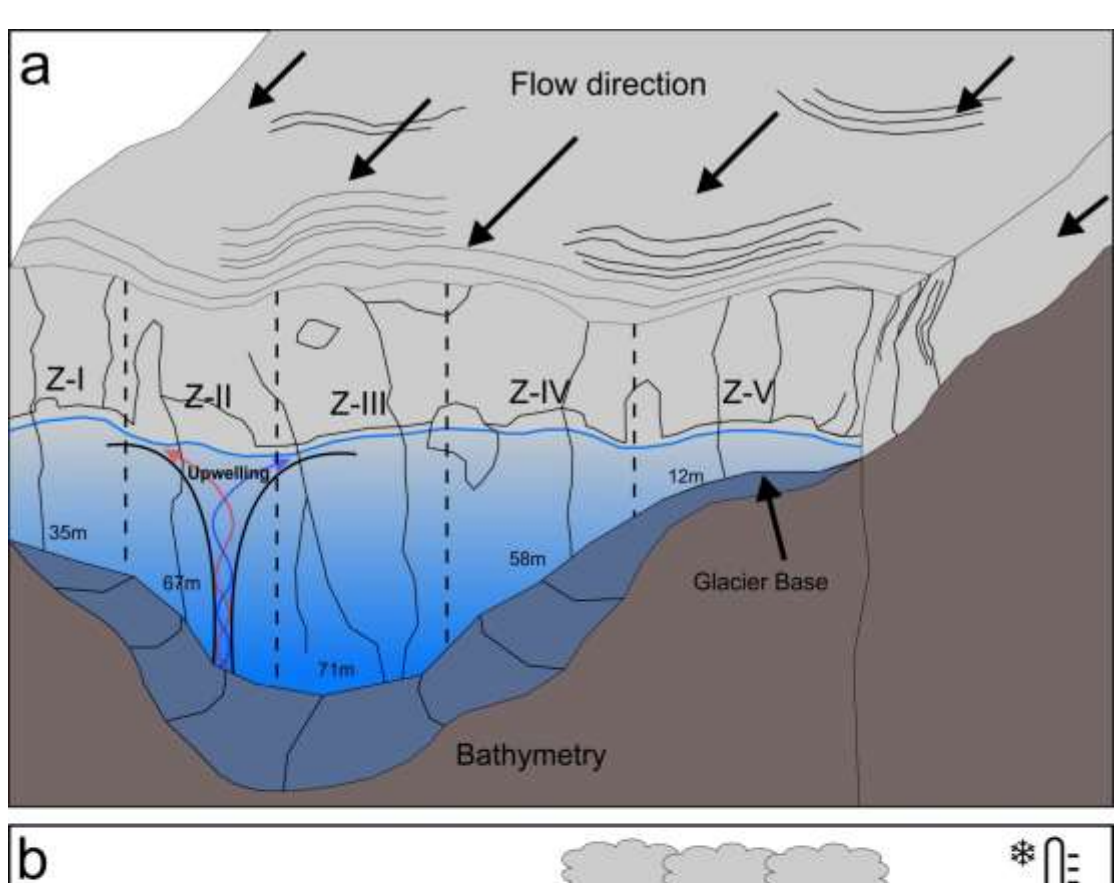


Fig. 6. Schematic showing processes influencing calving at the ice/ocean interface of marine-terminating glaciers. (a) Front view. (b) Side View



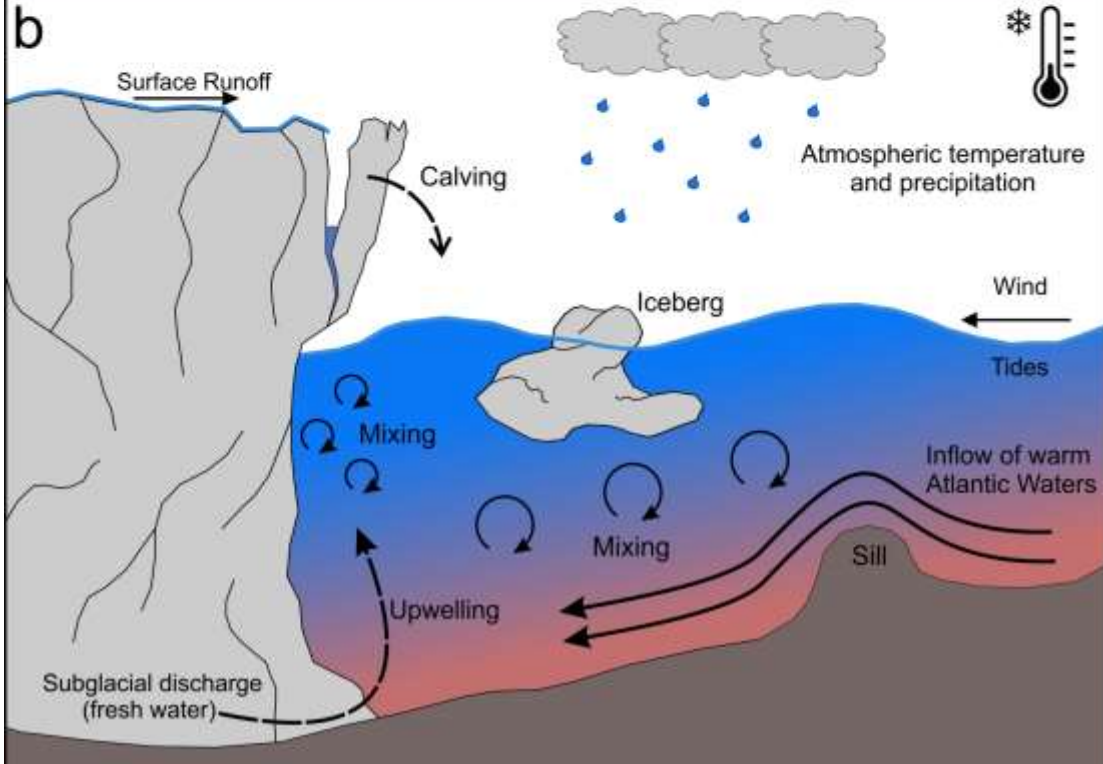


Fig. 7. Influence of the tidal cycle on calving variability at Hansbreen, July 2016. (a) Percentage of calving events occurring during ebb and flood tides, categorized into three calving types: waterline, icefall and sheet collapse. (b) Number of waterline calving events as a function of tidal amplitude. (c) Percentage of waterline events during ebb and flood tides, classified by terminus zones.

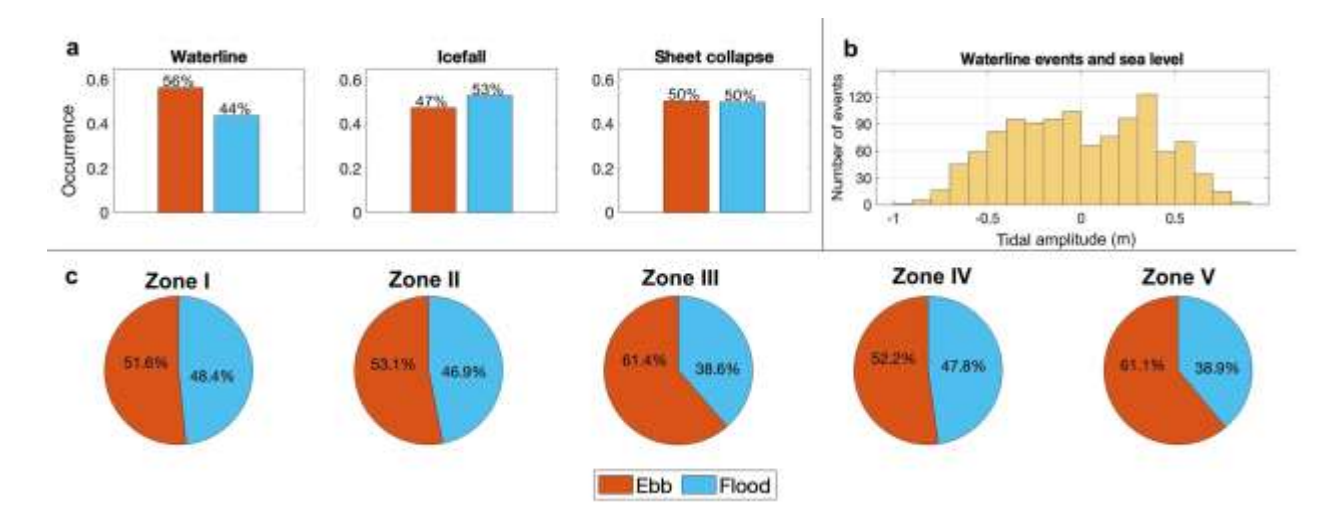
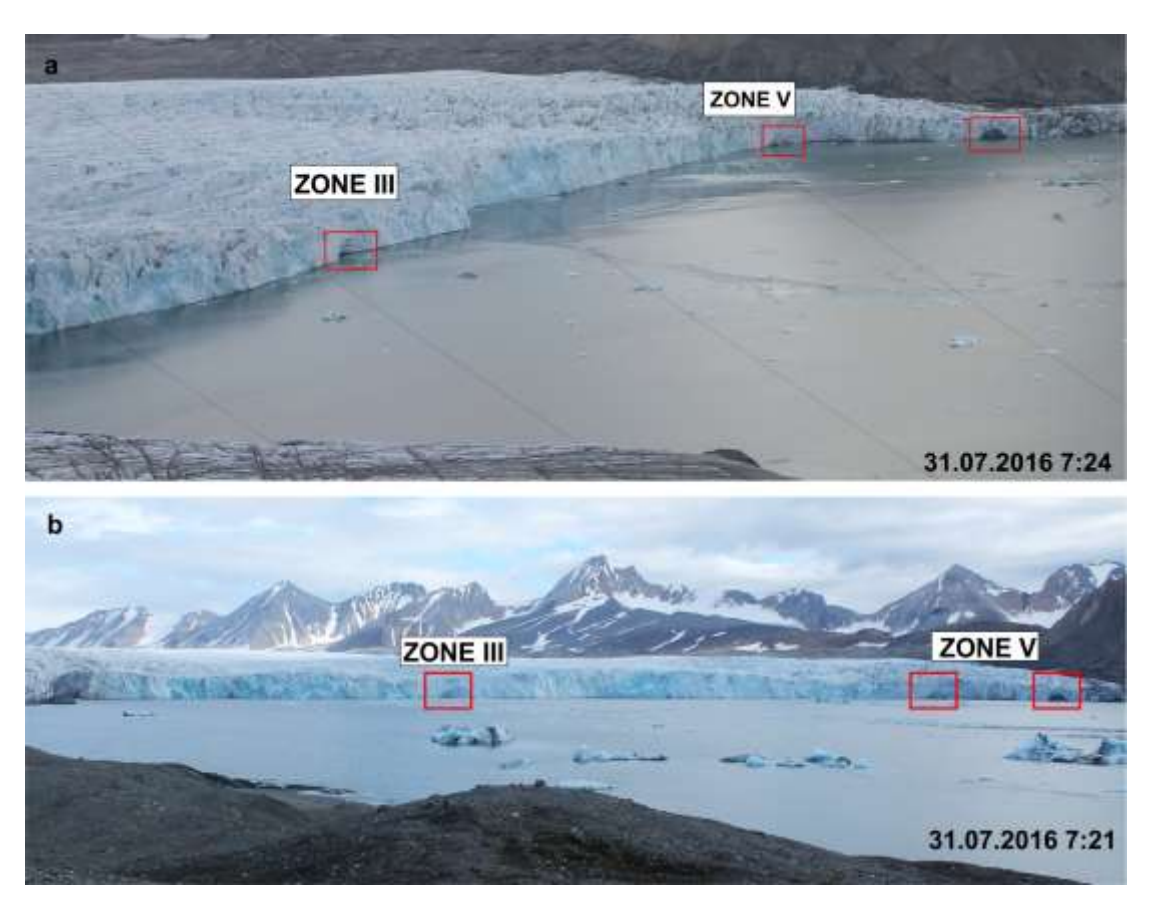


Fig. 8. Hansbreen front from two different time lapse cameras on 31 Jul 2016, showing three delineated caves - one in zone three and two in zone five. (a) Oblique View 7:24 am (b) Perpendicular View 7:21 am



TABLES

Table 1. Estimated volume range for calving size classes.

Class	Relative height (% of 30 m)	Height of the exposed area H (m)	Estimated Volume H ³ (m ³)
1	<25 %	<7.5	<400
2	25–50 %	7.5–15	400-3,000
3	50–75 %	15–22.5	3,000-11,000
4	>75 %	>22.5	>11,000